A *CHANDRA* SURVEY OF NEARBY SPIRAL GALAXIES. I. POINT SOURCE CATALOGS

R. E. KILGARD,[1,2] J. J. COWAN,[3] M. R. GARCIA,[1] P. KAARET,[1] M. I. KRAUSS,[1,4] J. C. McDOWELL,[1] A. H. PRESTWICH,[1] F. A. PRIMINI,[1] C. J. STOCKDALE,[5] G. TRINCHIERI,[6] M. J. WARD,[2] AND A. ZEZAS[1]

ABSTRACT

Emission from discrete point sources dominates the X-ray luminosity in spiral galaxies. We present results from a survey of 11 nearby, nearly face-on spiral galaxies with the *Chandra X-ray Observatory*. These galaxies span the Hubble sequence for spirals, allowing insights into the X-ray source population of many diverse systems. In this paper, we present source lists for the 11 galaxies along with fluxes, luminosities, X-ray colors, and variability properties. We briefly discuss X-ray luminosity functions and how they relate to star formation of the host galaxies. We also discuss source colors and variability and what these can tell us about the composition of the X-ray source population.

Subject headings: catalogs — galaxies: spiral — surveys — X-rays: galaxies

Online material: color figures

1. INTRODUCTION

The study of X-ray emission from galaxies has advanced greatly since the days of the *Einstein Observatory*. It is now well established that the emission consists of primarily two components: discrete sources and diffuse emission from hot gas and unresolved sources. The discrete sources are mostly composed of X-ray binaries and supernova remnants (for a good review of progress from the *Einstein* era, see Fabbiano 1989). However, with the limited spatial resolution of observatories prior to *Chandra* it was difficult, if not impossible, to clearly distinguish the point source population from diffuse emission due to hot gas in galaxies beyond a few megaparsecs. Now, with the unprecedented spatial resolution of *Chandra*, it is possible to separate even very closely spaced point sources and easily distinguish them from surrounding diffuse emission, and reach much lower sensitivity limits than was previously possible.

With this improved view of galaxies in the X-ray band, it becomes possible to answer many questions about the X-ray source population, such as, what are the X-ray point sources and what is their contribution to the total X-ray emission of galaxies? How does this change with galaxy size, Hubble type, or star formation rate (SFR)? What are the enigmatic ultraluminous X-ray sources (ULXs), and how common are they in normal galaxies? What is the characteristic shape of the X-ray luminosity function, how does that change with Hubble type or source type, and what does that tell us about the star formation history of the galaxy?

Much work has been done along these lines for individual galaxies since the launch of *Chandra*. For example, the source populations of individual normal spiral galaxies have been examined in great detail (e.g., M81, Swartz et al. 2003), as well as the X-ray properties of starbursts (e.g., the Antennae, Fabbiano

et al. 2001 and subsequent papers) In addition, catalogs of interesting sources have become available (e.g., ULXs, Colbert & Ptak 2002). In Kilgard et al. (2002), we showed that starburst galaxies have flatter discrete source luminosity function (LF) slopes than do normal spirals. Using simple population synthesis models, we argued that the steeper LF implies a more evolved X-ray source population. More recently, Colbert et al. (2003) have presented an analysis of the global X-ray properties of 32 nearby galaxies, suggesting that there is a correlation between total X-ray point source luminosity and star formation rate. A detailed review of galaxy observations thus far with *Chandra* is presented in Fabbiano & White (2005).

However, none of these projects have aimed to classify the point source population of galaxies in a systematic way. In an attempt to address this issue, we embarked on a *Chandra* AO2 large project to observe a sample of nearby, face-on spiral galaxies spanning the Hubble sequence. The main purpose of this work is to classify the discrete X-ray point source population. In this paper, the first in a series, we present source lists for our sample of galaxies, together with fluxes, X-ray colors, and information about source variability. We also present luminosity functions and X-ray and optical images obtained as part of the survey. In future papers, we will discuss the X-ray colors and variability of sources in greater detail, spectral analysis of the bright point source population, and more complete multiwavelength studies of counterparts and environments of X-ray sources.

In § 2, we discuss the selection of our sample and data reduction. In § 3, we present notes on individual galaxies, including their cumulative X-ray luminosity functions and X-ray and optical images. In § 4, we present discussions on luminosity functions and source variability and colors (see Figs. 1, 2, and 3, respectively). In § 5, we present conclusions of our work to date. In § 6, we present the source catalog.

2. DATA ANALYSIS

2.1. *Sample Selection*

Our sample is shown in Table 1. It is derived from the Nearby Galaxies Catalog (Tully 1988) and consists of galaxies spanning the Hubble sequence for spirals (types 0–7), inclinations $i < 35°$, distances $R \lesssim 10$ Mpc, and low Galactic extinction

[1] Harvard-Smithsonian Center for Astrophysics, 60 Garden Street, Cambridge, MA 02138.

[2] University of Leicester.

[3] Department of Physics and Astronomy, University of Oklahoma, 440 West Brooks, Room 131, Norman, OK 73019.

[4] Department of Physics, Massachusetts Institute of Technology, 77 Massachusetts Avenue, Cambridge, MA 02139.

[5] Naval Research Laboratory.

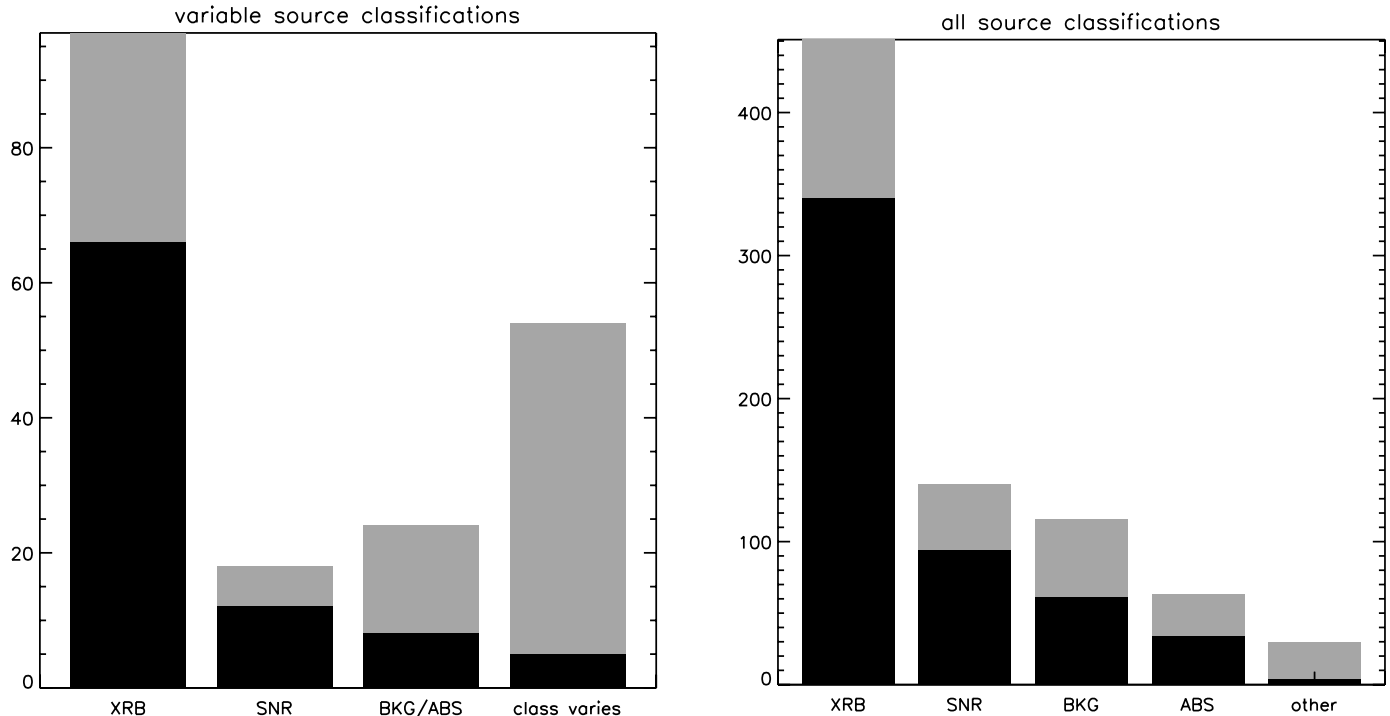[6] Brera Astronomical Observatory, Via Brera 28, Milan 20121, Italy.

Fig. 1.—X-ray point source classifications for all sources in the 11 survey galaxies, using the color classification scheme of Prestwich et al. (2003). The left-hand plot shows source classifications for the sources whose fluxes vary at the 90% level between *Chandra* observations. The black bars indicate sources with greater than 25 counts in both observations. The right-hand plot indicates source classifications for all sources, taken from the longer *Chandra* observation of each galaxy or, for observations of approximately equal length, the observation for which colors were better determined. Black bars indicate sources with more than 25 counts.

($N_H < 5 \times 10^{20}$ cm^{-2}). Note that two of the galaxies, NGC 1291 and NGC 4314, have distances slightly larger than 10 Mpc, but they were felt to be strong candidates for other reasons; NGC 1291 (an S0 galaxy) because of the already present archival data and the sparsity of nearby early-type spirals, and NGC 4314 because of the large number of detailed optical studies available in the literature. In addition, NGC 278 has an $N_H = 1.29 \times 10^{21}$ cm^{-2}, but we relaxed this requirement because the only other Sb galaxy with $i < 25°$ within 15 Mpc in the Nearby Galaxies Catalog is NGC 1068, which has an extremely luminous Seyfert nucleus that is very piled up in *Chandra* observations, leading to confusion in the nuclear region and along the readout streaks.

2.2. *X-Ray Data Analysis*

All observations were performed on the ACIS instrument with the aim point falling on the back-illuminated S3 chip. This was chosen because the S3 chip has excellent low-energy response and better sensitivity, and it does not suffer as much form the effects of charge transfer inefficiency (CTI) as do the front-illuminated CCDs. In addition, the calibration of the S3 chip is more complete than that of the other ACIS chips. The observations were conducted in regular graded/faint mode with the standard 3.2 s frame time and six chips on (I2, I3, S2, S3, S4, S5). The one exception is M94, which was observed in a 1/4 subarray on S3 during the longer (49 ks) observation and a 1/8 subarray on S3 during the shorter (2 ks) observation. This yields much shorter frame times of 0.84 and 0.42 s (respectively) and was done to mitigate the effects of pile-up in data from the bright nuclear source, but it reduces the field of view to a strip of $8' \times 2'$ for the 1/4 subarray and $8' \times 1'$ for the 1/8 subarray. The fraction of D_{25} covered in each galaxy is listed in Table 1. Analyses were performed using the *Chandra* Interactive Analysis of Observations software (CIAO) version 2.2.1 and the *Chandra* Calibration database ver-

sion 2.11. Standard data processing was performed at the *Chandra* X-ray Center. Data were then reprocessed using the latest calibration files available, utilizing new gain maps, improved plate scale,[7] and applying PHA randomization. The S4 data were additionally cleaned using the tool `destreak`, which removes linear streaks that are due to a detector artifact.[8] For the purposes of source detection, the observations were screened for periods of high background due to increased solar activity, and background levels above the mean level in each observation by 20% were excluded. All the observations of each galaxy were then merged using the CIAO script `merge_all`, which reprojected the events files into a common coordinate plane and created a merged events list (exposure maps were not used in this analysis). These merged data were only used for the purpose of source detection. Source lists were constructed using wavdetect (Freeman et al. 2002), the Mexican-hat wavelet source detection routine that is part of CIAO. The detection was run on full-resolution images with a restricted energy filter of 0.3–6.5 keV using wavelet scales of 2, 4, 8, and 16 pixels and again in the energy range 0.5–6.5 keV using scales of 1, 2, 4, 8, and 16 pixels, with the latter used in regions where confusion due to unresolved emission or close spacing of sources may be a problem. The wavdetect significance threshold was 10^{-6}, and sources with significance of less than 3 were excluded unless they were visibly obvious point sources. The wavdetect encircled energy fraction was set to 0.393, corresponding to the 1 σ integrated volume of a two-dimensional Gaussian, with PSF size computed at 1.4967 keV. This combination of energy bands and wavelet scales yielded the fewest

---

[7] The new plate scale is a consequence of a better calculation of the *Chandra* focal length and was implemented in the CALDB ver. 2.9, see http://cxc.harvard .edu/cal/Hrma/optaxis/platescale/foc_len_public.html.

[8] For details on `destreak`, see http://cxc.harvard.edu/ciao/download/scripts/ destreak.ps.

Disk-dominated systems

$\Gamma_{obs} = 1.04 \pm 0.10$
$\Gamma_{corr} = 1.17 \pm 0.14$

Bulge-dominated systems

$\Gamma_{obs} = 1.19 \pm 0.17$
$\Gamma_{corr} = 1.14 \pm 0.17$

Star-forming systems

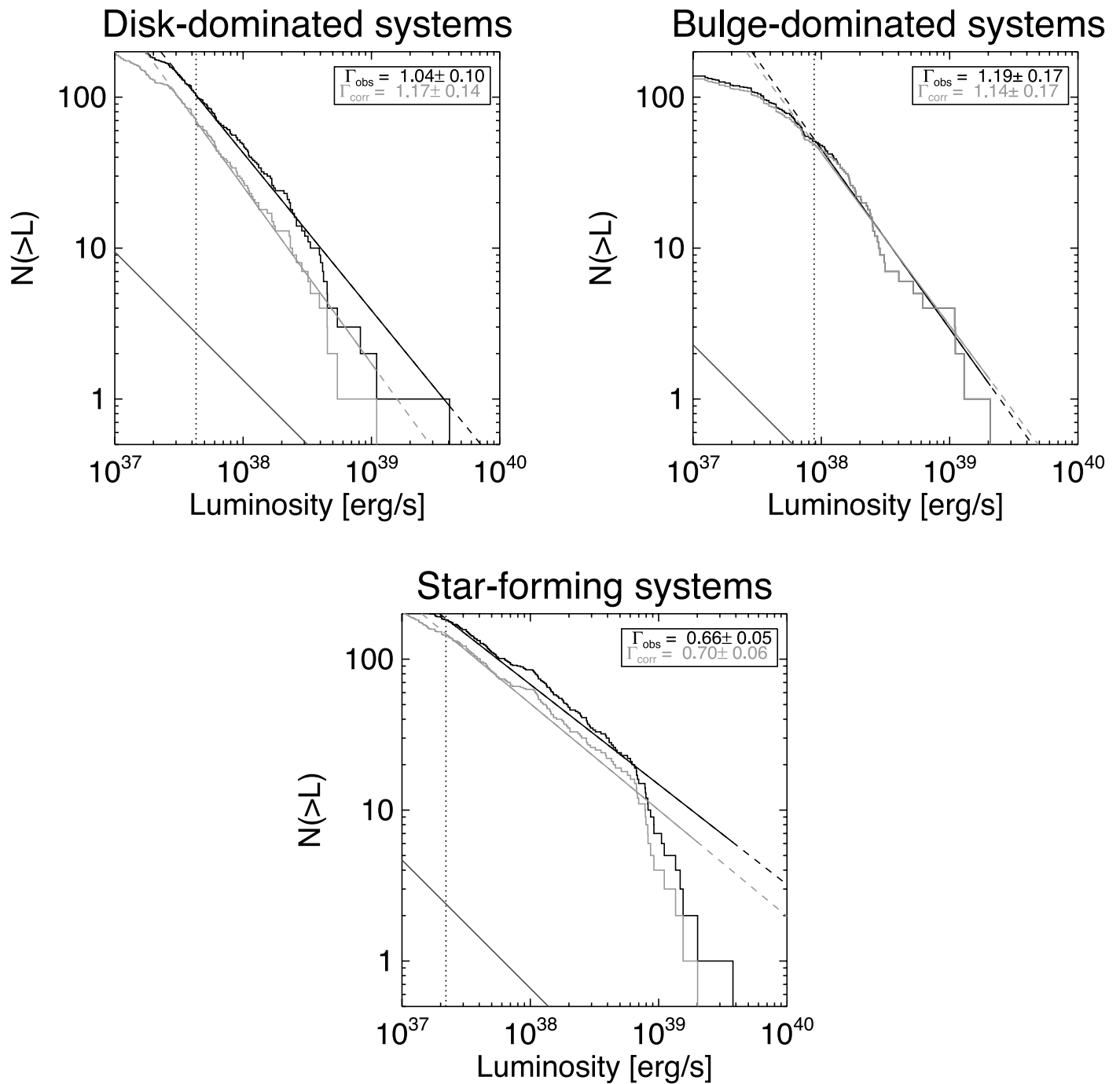$\Gamma_{obs} = 0.66 \pm 0.05$
$\Gamma_{corr} = 0.70 \pm 0.06$

FIG. 2.—Cumulative luminosity function of the X-ray point sources in galaxy subsets. The black curves indicate the complete data plus background LFs and the best-fit single power law. The blue curves indicate the background-subtracted data LF and best-fit single power law. The red curve indicates the ideal background LF. The disk-dominated galaxies are M74, NGC 3184, M101, and IC 5332; the bulge-dominated galaxies are NGC 278, NGC 1291, NGC 2681, and NGC 4314; and the systems with high star formation are M94, M51, and M83. [*See the electronic edition of the Journal for a color version of this figure.*]
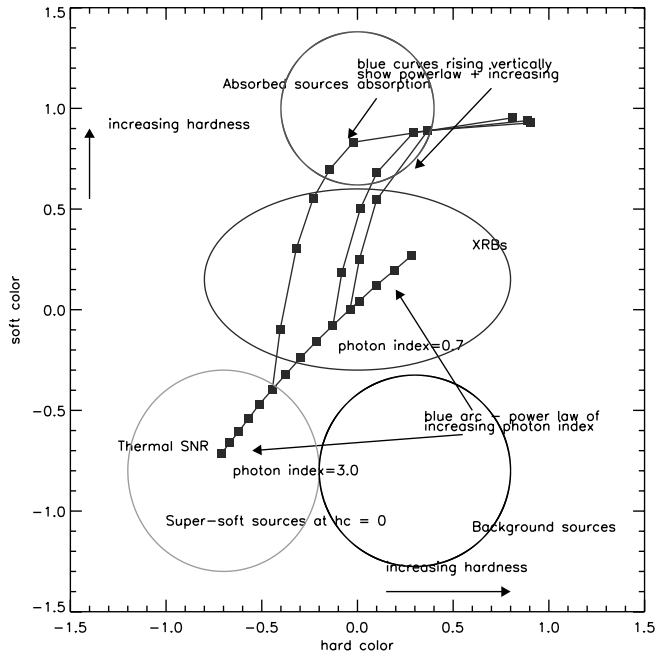
Fig. 3.—Color-color diagram as suggested by Prestwich et al. (2003). The blue lines represent power laws of decreasing photon index (hardening spectrum). As absorption is added, sources travel up and to the right along the curves. Ellipses outline the major source categories. Though we use different color definitions from Prestwich et al. (2003), we plot the same curves here as their Fig. 4 for reference. [*See the electronic edition of the Journal for a color version of this figure.*]

band (H) 2–8 keV, and the total band (T) of 0.3–8 keV. Events below 0.3 keV and above 8 keV were excluded because they tend to be dominated by background and intrinsic detector noise. Sherpa is used due to potential overlaps in PI to energy mapping. For example, if a PI channel is defined as having low- and high-energy bounds of 0.98 and 1.02 keV, respectively, then any counts that fall within that PI channel will be extracted in both the 0.3–1 keV and 1–2 keV bands. For each source, we determine the PI channels corresponding to the energies 0.3, 1.0, 2.0, and 8.0 keV. We will refer to them as PI channels A, B, C, and D, for convenience. Counts are then extracted in the PI regions A to B, B+1 to C, C+1 to D, and A to D.

Hardness ratios were then calculated from these values using the following form:

$$HC = \frac{(H-M)}{(H+M)} \tag{1}$$

and

$$SC = \frac{(M-S)}{(M+S)}, \tag{2}$$

with errors based on standard error propagation:

$$HCERR = \frac{2\sqrt{H^2 \times MERR^2 + M^2 \times HERR^2}}{(H+M)^2} \tag{3}$$

and

$$SCERR = \frac{2\sqrt{M^2 \times SERR^2 + S^2 \times MERR^2}}{(M+S)^2}, \tag{4}$$

where the error on the counts was taken to be the statistical error using the Gehrels approximation (Gehrels 1986):

$$ERR = 1 + \sqrt{COUNTS + 0.75}. \tag{5}$$

These values are presented in the catalog table for each galaxy. For the sources that fall on the front-illuminated CCDs, weights were applied to correct the source counts to the value expected on the S3 chip using a conversion factor equal to the ratio of effective areas of the front-illuminated CCDs and the S3 aim point. A different conversion factor was used for each color band. These weighted counts were used for color calculation, not for the count values listed in the catalog and not for the flux and luminosity calculations where the differences are taking into account by appropriate response files. The colors were then used to determine initial classifications for each source. Ideally, one would consider the spectral shape of the source in determining the correction factor, but most of the sources in our sample have insufficient counts to determine the spectral shape.

We have changed our color definitions from the work of Prestwich et al. (2003) to be more consistent with other work in the literature. We present our coarse bins in Table 2. In Figure 3, we show the curves of constant photon index and the Galactic reference sources from Prestwich et al. (2003), plotted in the color-space defined in Table 2. We choose our color bands to include all the sources as classified by Prestwich et al. (2003), and, as we are interested here in only bulk trends across our sample, we include both high- and low-mass X-ray binaries in the same bin.

spurious detections and found all visually obvious point sources. The output source regions were visually inspected to remove the artifacts that sometimes occur with wavdetect: regions where the ellipse minor axis is zero, regions containing two sources, and sources detected twice. Sources outside the galaxy D_{25} ellipses were also removed. Each source has been assigned a name following the *Chandra* naming convention. This is presented in the catalog tables for each galaxy. If this or another name has been used for the source in an existing publication, it is also noted in the table. For galaxies whose D_{25} radii extended beyond the S3 chip, source detection was performed on flanking chips as necessary. Details are given in the notes on individual galaxies.

For each source and each observation, pulse invariant (PI) spectra were extracted from the full energy range (0.1–11 keV), reprocessed events lists and response matrix files (RMFs) and ancillary response functions (ARFs) were constructed. The source extraction regions were taken to be the wavdetect default output. When the source was detected in more than one run of wavdetect, the smaller ellipse was used. Corresponding background spectra were extracted for each source, and background responses were generated. The ARFs were then corrected for the ACIS low-energy degradation using the tool `corrarf`.[9] The region for each background spectrum was taken to be an ellipse with radius equal to 4 times the source radius and excluding the source regions and any other overlapping source regions. To limit contamination from unresolved emission not characteristic of the background at the source, the background ellipse radii were not allowed to exceed 50 pixels (about 25″).

Background subtracted counts in four bands were determined for each source using the CXC spectral fitting tool Sherpa: a soft band (S) of 0.3–1 keV, medium band (M) of 1–2 keV, hard

---

[9] The `corrarf` tool, written by Alexey Vikhlinin, can be found at http://hea-www.harvard.edu/~alexey/.

TABLE 1
GLOBAL PROPERTIES OF SAMPLE GALAXIES

Galaxy	Morphology	i (deg)	R (Mpc)	D_{25} (arcmin)	Frac. D_{25} 1/2/Total	N_H (10^{20} cm^{-2})	Obs. ID 1/2	Duration 1/2 (s)	Γ 1/2	σ 1/2	GOF 1/2[a]	Number of Sources	Number of ULXs
NGC 278................................	Sb	0	8.5[b]	2.1	1.00/1.00/1.00	12.9	2055/2056	38258/37269	0.89/1.03	0.33/0.39	0.55/0.22	14	1
M74 (NGC 628)	Sc	0	8.8[b]	10.5	0.75/0.74/0.88	4.81	2057/2058	46352/46169	1.03/1.08	0.16/0.15	1.96/1.79	67	1
NGC 1291.............................	S0/a	28	8.9[c]	9.8	0.76/0.87/0.94	2.24	795/2059	39168/36533 (22906)[d]	0.74/1.01	0.09/0.14	1.85/1.56	93	2
NGC 2681.............................	S0/a	0	9.2[e]	3.6	1.00/1.00/1.00	2.48	2060/2061	80898/78977	0.63/0.62	0.15/0.15	1.46/0.67	23	1
NGC 3184.............................	Scd	26	11.1[f]	7.4	1.00/1.00/1.00	1.15	805/1520	42122/23731	1.11/0.84	0.21/0.15	1.03/1.31	49	0
NGC 4314.............................	Sa	15	12.8[g]	4.2	1.00/1.00/1.00	1.62	2062/2063	16075/16044	1.20/1.19	0.38/0.36	0.61/0.89	19	0
M94 (NGC 4736)...................	Sab	33	4.1[h]	11.2	0.18/0.09/0.20	1.44	310/808	47366/2314	0.48/0.69	0.08/0.21	1.18/0.66	50	0
M51 (NGC 5194/95).............	Sbc	20	6.2[i]	11.2	0.88/0.88/0.88	1.53	354/1622	14865/26808	0.83/0.72	0.13/0.09	0.83/1.01	116	3
M83 (NGC 5236)...................	Sc	24	4.5[j]	12.9	0.77/0.77/0.99	3.70	793/2064	50978/9845	0.58/0.92	0.06/0.12	1.38/0.93	131	3
M101 (NGC 5457)................	Scd	0	7.2[k]	28.8	0.51/0.51/0.78	1.15	934/2065	98244/9633	0.54/0.73	0.04/0.15	1.58/0.97	208	3
IC 5332	Sd	25	9.4[l]	7.8	1.00/1.00/1.00	1.38	2066/2067	52134/55247	1.12/1.26	0.22/0.23	1.59/1.04	50	0

[a] An estimate of the goodness of fit derived from Monte Carlo simulations as defined in § 2.2. The quantity measures the deviation as compared with that from a pure power-law distribution; thus, the quantity should approach unity as the data approach a pure power-law distribution.

[b] Huchra et al. (1999).

[c] de Vaucouleurs (1975).

[d] This observation contains a large flare starting at 23 ks. The flare data were filtered out for the purposes of analysis.

[e] de Vaucouleurs et al. (1991).

[f] Leonard et al. (2002).

[g] Benedict et al. (1996).

[h] Mulder & van Driel (1993).

[i] Feldmeier & Ciardullo (1997).

[j] Thim et al. (2003).

[k] Stetson et al. (1998).

[l] de Costa et al. (1991).

TABLE 2
COLOR-COLOR CLASSIFICATIONS

Classification	Definition
Supernova remnant	HC < −0.2, SC < −0.3
X-ray binary.................................	−0.8 < HC < 0.8, −0.3 < SC < 0.6
Background source	HC > −0.2, SC < −0.3
Absorbed source	SC > 0.6
Indeterminate soft source.............	HC < −0.8, −0.3 < SC < 0.6
Indeterminate hard source............	HC > 0.8, −0.3 < SC < 0.6
Supersoft source..........................	M = 0, H = 0

Fluxes and luminosities were calculated in the 0.3–8 keV band. Since most sources do not have sufficient counts for detailed spectral analysis, it is necessary to assume some spectral model for flux and luminosity calculations. For each source, fluxes were calculated for three assumed spectral models: a simple power law with $\Gamma = 1.5$ and photoelectric absorption, a disk blackbody with $T_{in} = 1.0$ keV and photoelectric absorption, and a thermal bremsstrahlung model with $kT = 5.0$ keV and photoelectric absorption. These models were chosen as characteristic of the best-fit spectra to bright point sources in the sample. In all cases, the absorption was set to the Galactic value; since our galaxies are face-on, line-of-sight absorption in the host galaxy should be minimal. Fluxes were then calculated in Sherpa by rescaling the normalization of the models to the observed count rates. Luminosities were calculated using the distances listed in Table 1. This method of normalization to fixed model parameters occasionally allows some model types to be rejected for any given source. For example, if the source spectrum is drastically different from a 1.0 keV disk blackbody, the normalization (being the only free parameter) will reach the maximum or minimum allowed value. This will return a physically unrealistic flux as compared with the flux from a simple PIMMS calculation (e.g., the flux may be different by several orders of magnitude). The rejection of some models is potentially useful

in source classification. While we do not make use of this data here beyond presenting it in the source catalog, it will be utilized in future papers. In the source list tables, we list only the power-law fluxes and luminosities except where the power law can be rejected, in which case the model used is noted as a footnote. We also note sources that are apparently highly absorbed, where the medium and hard count bins contain the overwhelming majority of source counts.

Cepheid or other high-quality distance indicators were used, where available. However, only distances based on recessional velocities were available for several galaxies within the sample. Since all galaxies in our sample are nearby, distances from recessional velocities are not particularly accurate and, indeed, can be incorrect by a factor of 2 or more. Distances used and references can be found in Table 1. A Hubble constant value of 73 km s^{-1} Mpc^{-1} was used.

It should be noted that the detection threshold differs greatly between the FI and BI ACIS chips due to the considerably higher background on the BI chips, off-axis angle that increases the PSF size (primarily a consideration on the FI chips), and effective area. Since the detection limit is based on the significance of the source detection as computed by wavdetect, it is not a fixed flux. We must therefore consider the completeness limit when discussing, for example, luminosity functions. For sources that span multiple ACIS chips, we must assume the completeness limit for the FI CCDs. We define the completeness limit as the minimum luminosity at which a source is detected, with a wavdetect significance of at least 3, at the edge of the galaxy D_{25} ellipse. In the discussions of individual galaxies, we consider only those sources on the back-illuminated S3 chip unless otherwise noted.

Though the *Chandra* astrometry is generally good to ∼1″ on the aim point ACIS chip, the sources on the FI chips will have decreasing accuracy with increasing off-axis angle. In addition, our utilization of the newer plate scale produces a slight discrepancy between the coordinates in the literature for some of the sources and the coordinates presented here.
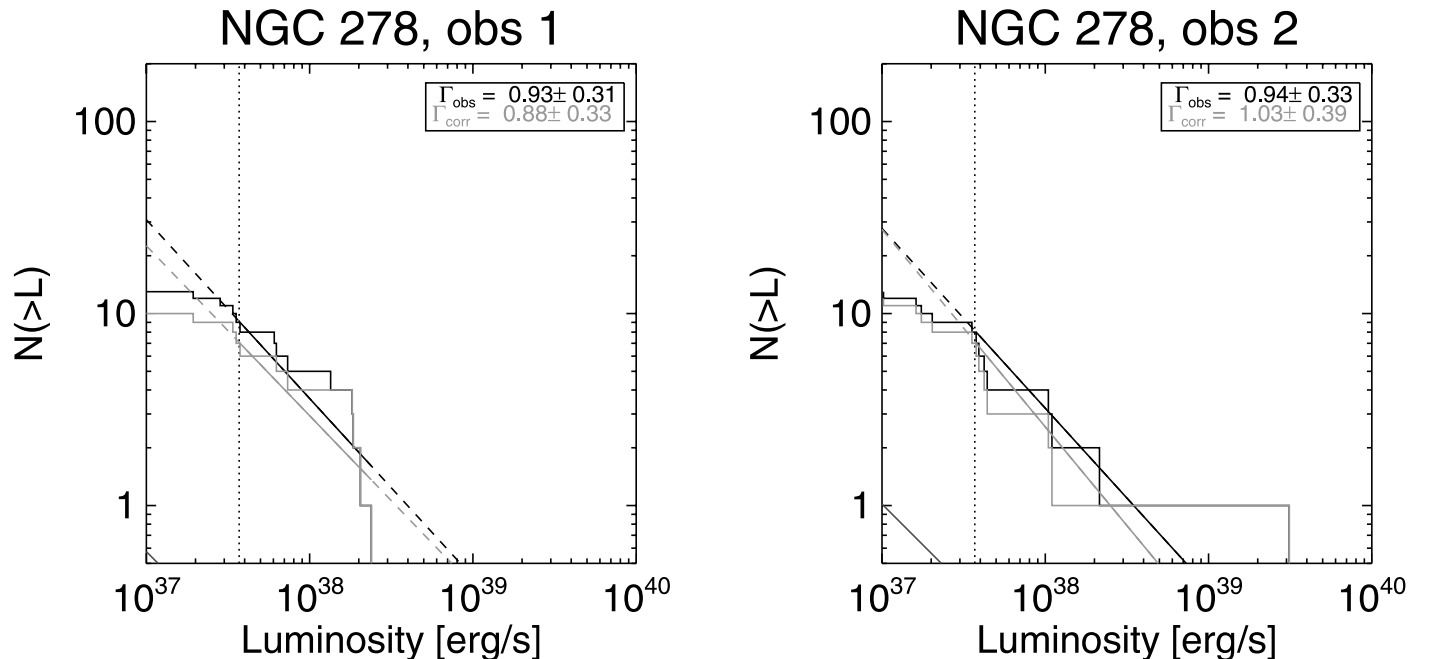

FIG. 4.—Cumulative luminosity function of the X-ray point sources in NGC 278. LFs for both *Chandra* observations are plotted. Solid lines indicate the range of data used for the fit. Nuclear sources and sources below the detection completeness limit are excluded. [*See the electronic edition of the Journal for a color version of this figure.*]
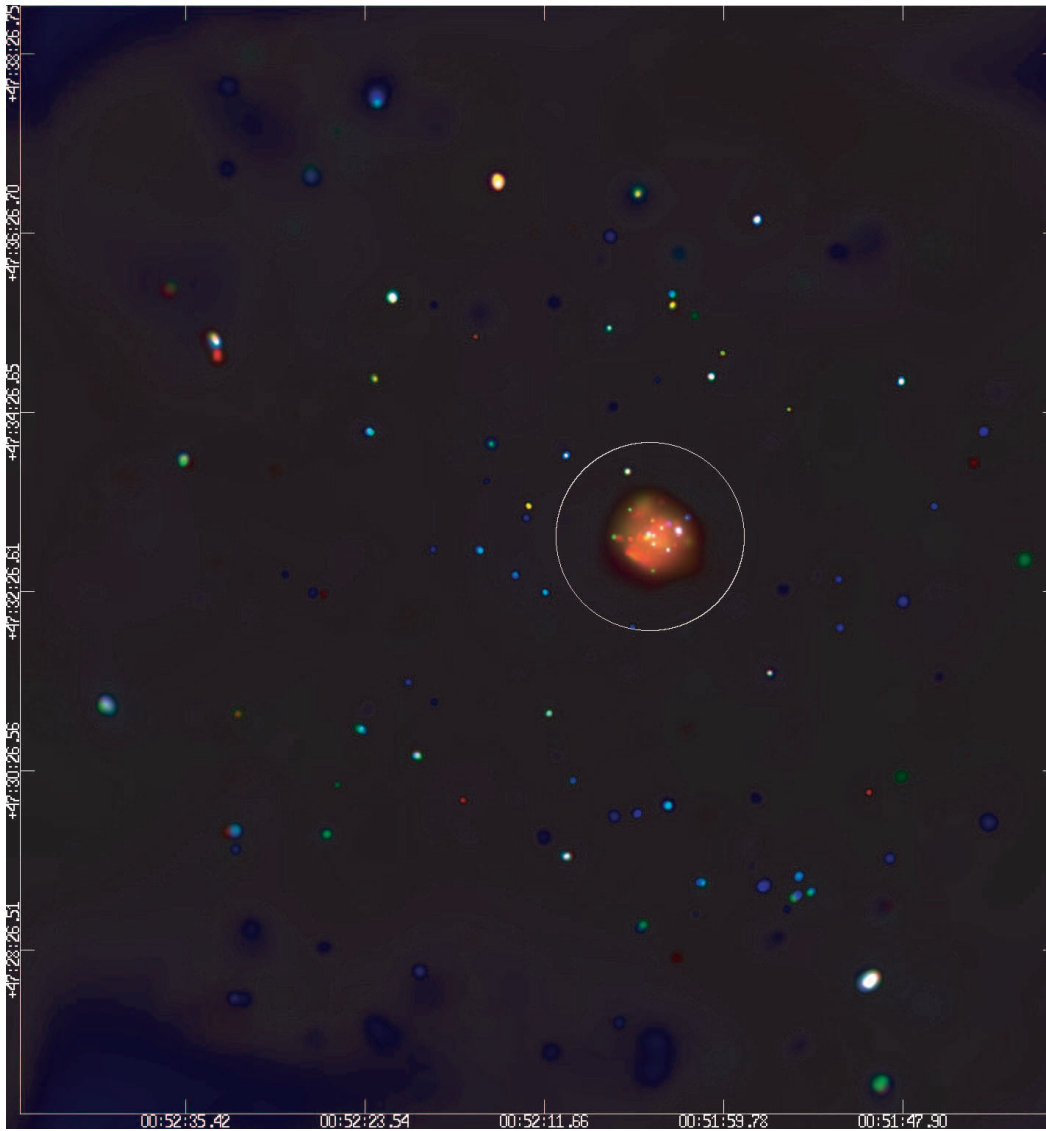
FIG. 5.—Merged *Chandra* observation of NGC 278. Adaptively smoothed. Red is 0.3–1 keV, green 1–2 keV, and blue 2–8 keV. Overplotted is the galaxy D_{25} ellipse.
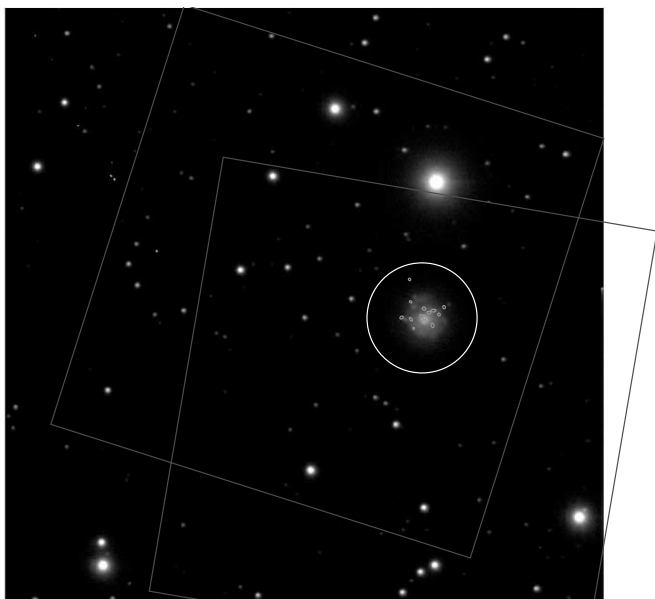

FIG. 6.—Optical image of NGC 278 with *Chandra* sources overlaid. The white circle is the D25 extent of the galaxy. The scale of the image is $4' \times 4'$. [*See the electronic edition of the Journal for a color version of this figure.*]
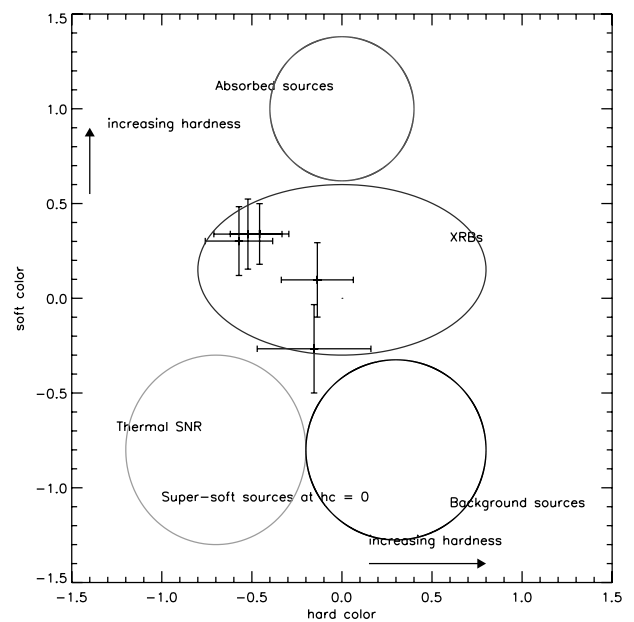

FIG. 7.—Color-color diagram of the X-ray point sources in NGC 278. Only sources with greater than 25 counts are included. The ellipses represent the approximate regions for source classification as defined in Prestwich et al. (2003). [*See the electronic edition of the Journal for a color version of this figure.*]

M74, obs 1

$\Gamma_{obs} = 0.92 \pm 0.12$
$\Gamma_{corr} = 1.03 \pm 0.16$

N(>L)

Luminosity [erg/s]

M74, obs 2

$\Gamma_{obs} = 0.95 \pm 0.13$
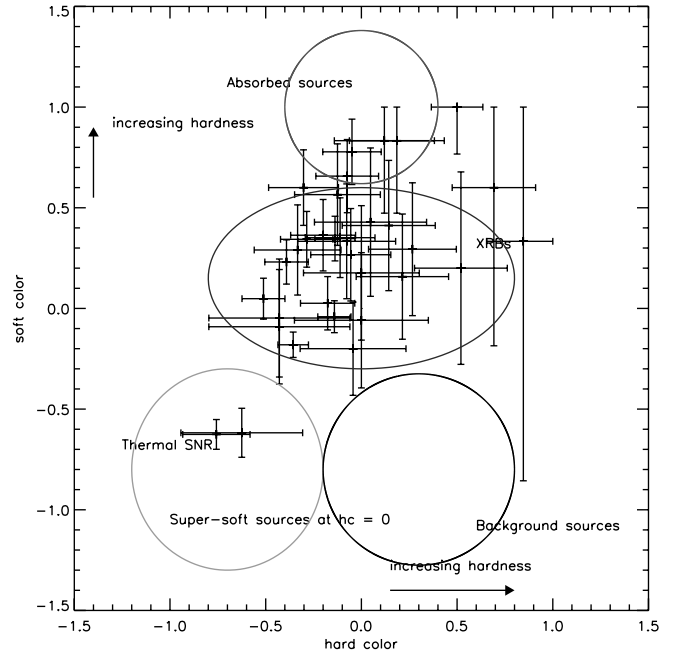$\Gamma_{corr} = 1.08 \pm 0.15$

N(>L)
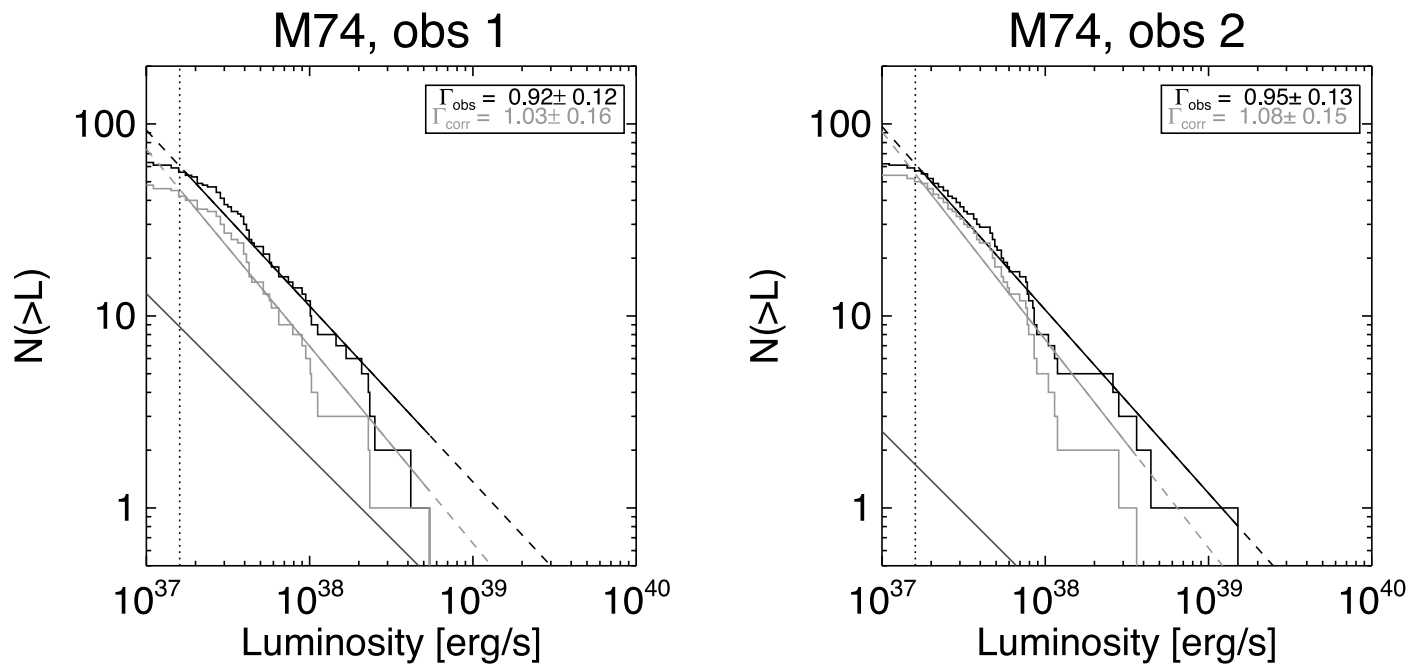
Luminosity [erg/s]

FIG. 8.—Cumulative luminosity function of the X-ray point sources in M74. [*See the electronic edition of the Journal for a color version of this figure.*]
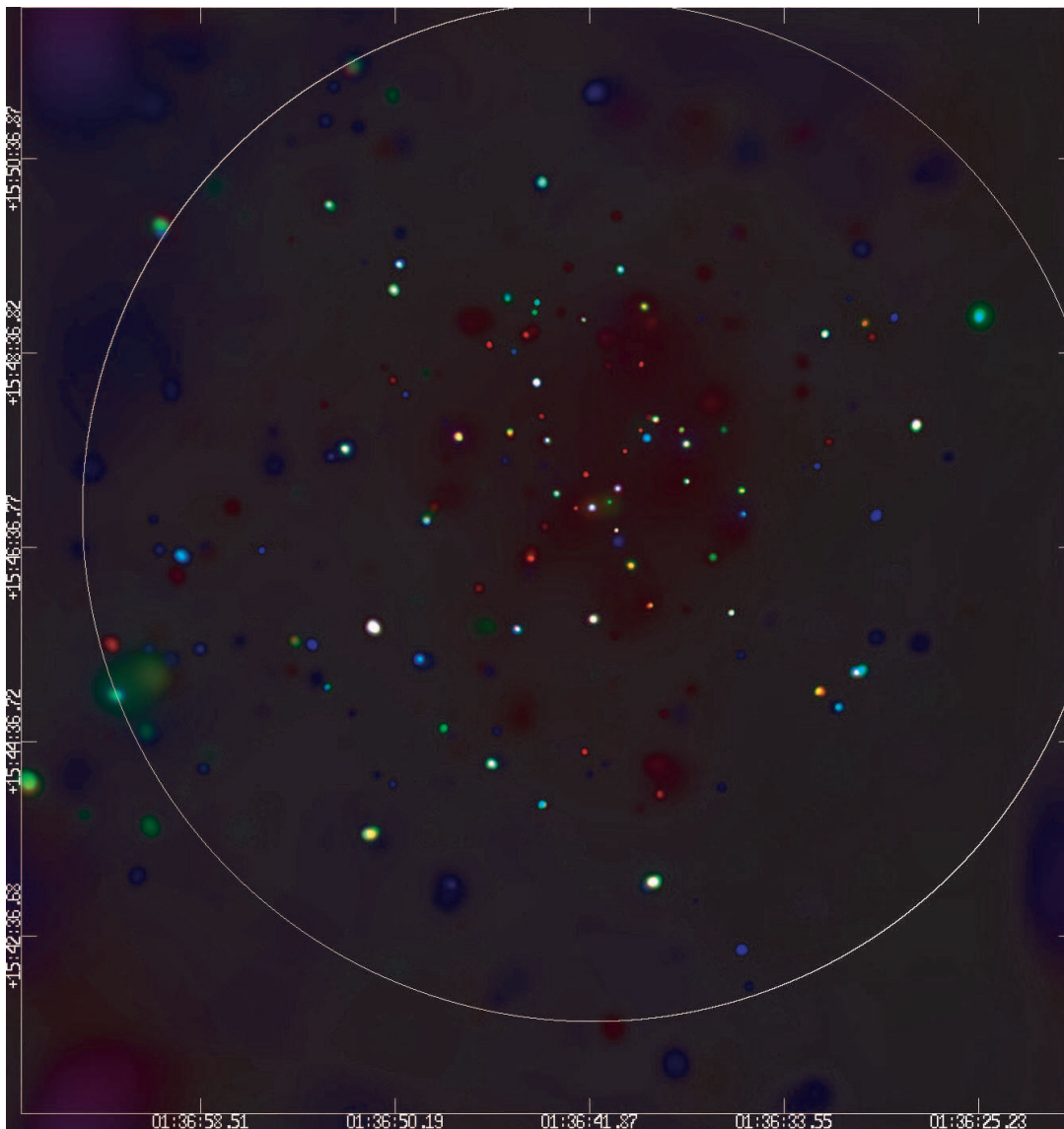
FIG. 9.—Merged *Chandra* observation of M74. Adaptively smoothed. Red is 0.3−1 keV, green 1−2 keV, and blue 2−8 keV.
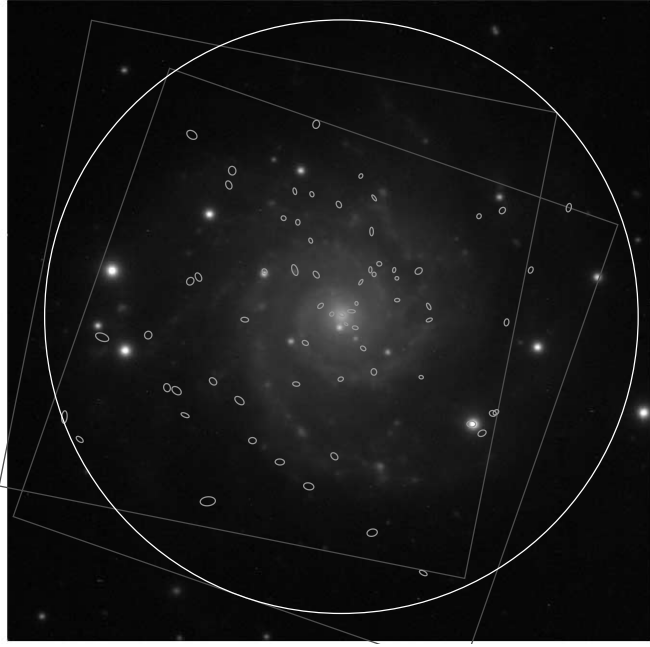
Fig. 10.—FLWO optical image of M74 with *Chandra* sources overlaid. The white circle is the D25 extent of the galaxy. The scale of the image is $10' \times 10'$. [*See the electronic edition of the Journal for a color version of this figure.*]

Fig. 11.—Color-color diagram of the X-ray point sources in M74. [*See the electronic edition of the Journal for a color version of this figure.*]

The cumulative luminosity functions for each observation of each galaxy are presented in the first figure in each subsection. In order to avoid incompleteness, we consider only the high-luminosity range of the luminosity functions. We set an overall conservative completeness limit determined by the data available for each galaxy. The completeness limits for each galaxy are cited in those galaxy subsections.

We derive power-law fits to the unbinned differential luminosity functions using a maximum likelihood statistic following Crawford et al. (1970). We evaluate the goodness of fit using a Monte Carlo technique. The fitted slopes, Γ, and estimate of

goodness of fit are shown in Table 1. In fitting the LFs, we include a background component from Giacconi et al. (2001), scaled to the area of each galaxy and the flux detection limit of each observation. For galaxies spanning more than one ACIS chip, we include a separate background component per chip, as both the area and the completeness limit will be different. The plots each show the complete data and best-fit LF slope (*black curve*), background-subtracted data and best-fit LF slope (*blue curve*), and slope indicating the distribution of background sources (*red curve*). The background is subtracted by simulating a random distribution of background sources (scaled as described above) and removing that sample distribution from the data.
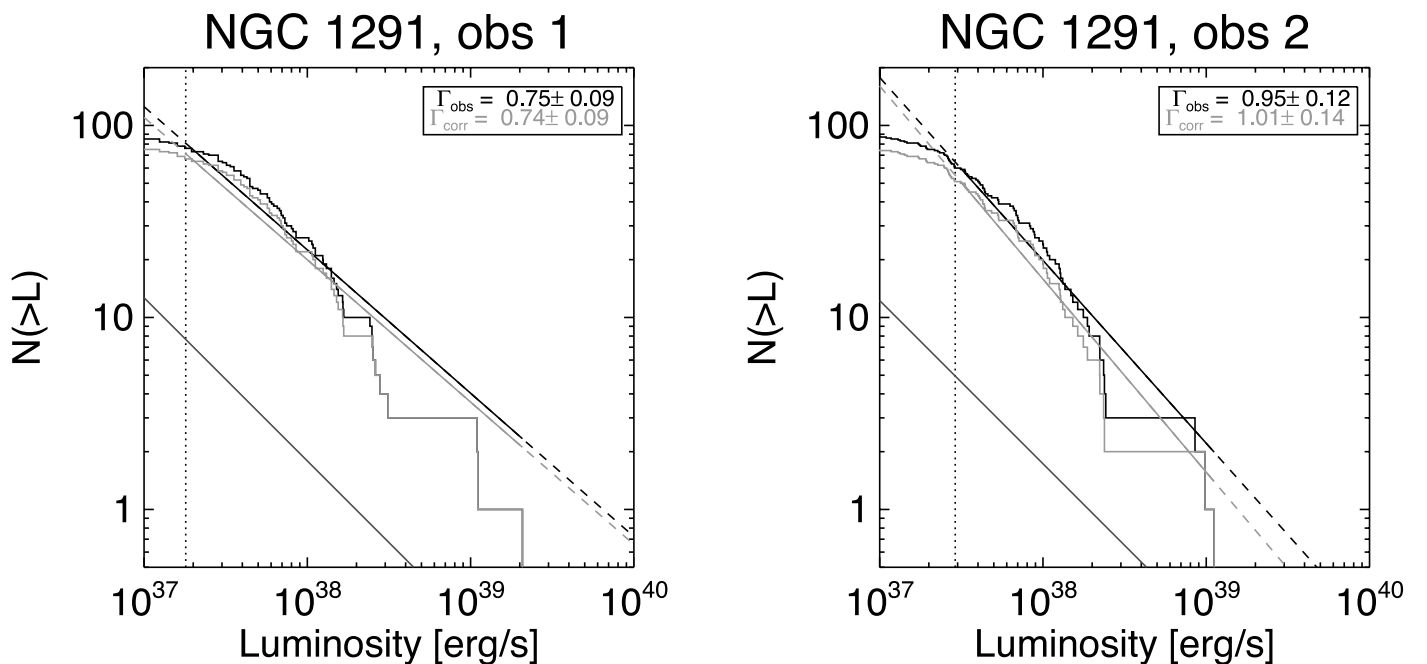

Fig. 12.—Cumulative luminosity function of the X-ray point sources in NGC 1291. [*See the electronic edition of the Journal for a color version of this figure.*]
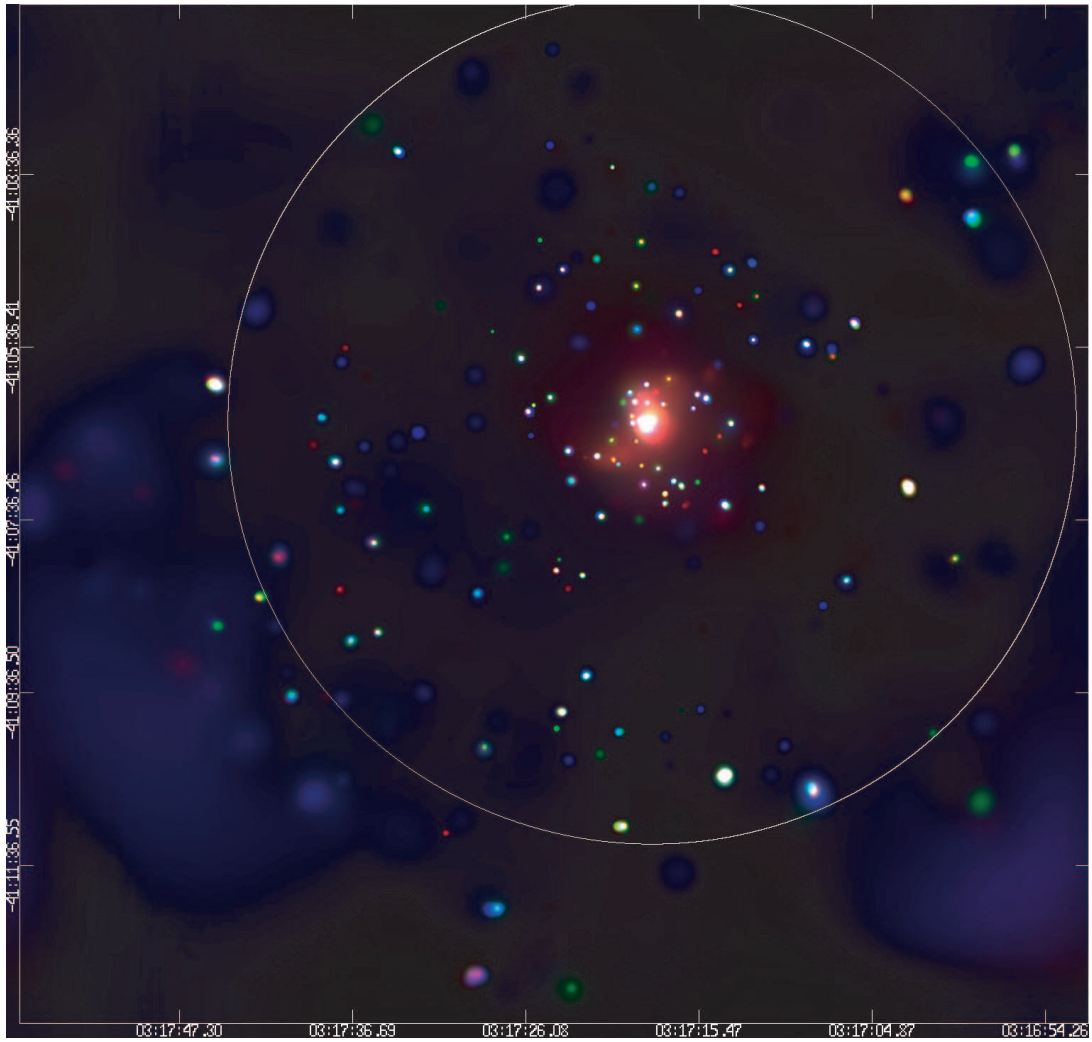
Fig. 13.—Merged *Chandra* observation of NGC 1291. Adaptively smoothed. Red is 0.3–1 keV, green 1–2 keV, and blue 2–8 keV.
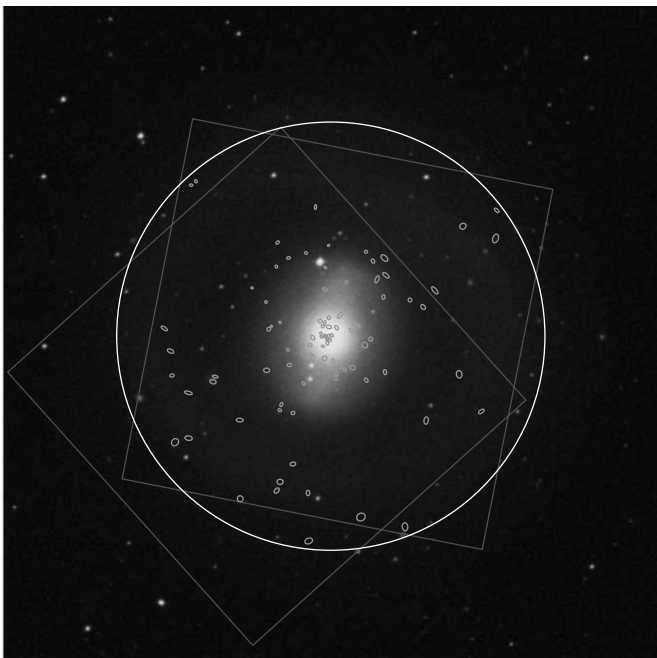

Fig. 14.—DSS optical image of NGC 1291 with *Chandra* sources overlaid. The white circle is the D25 extent of the galaxy. The scale of the image is $10' \times 10'$. [*See the electronic edition of the Journal for a color version of this figure.*]

Fig. 15.—Color-color diagram of the X-ray point sources in NGC 1291. [*See the electronic edition of the Journal for a color version of this figure.*]

NGC 2681, obs 1

NGC 2681, obs 2
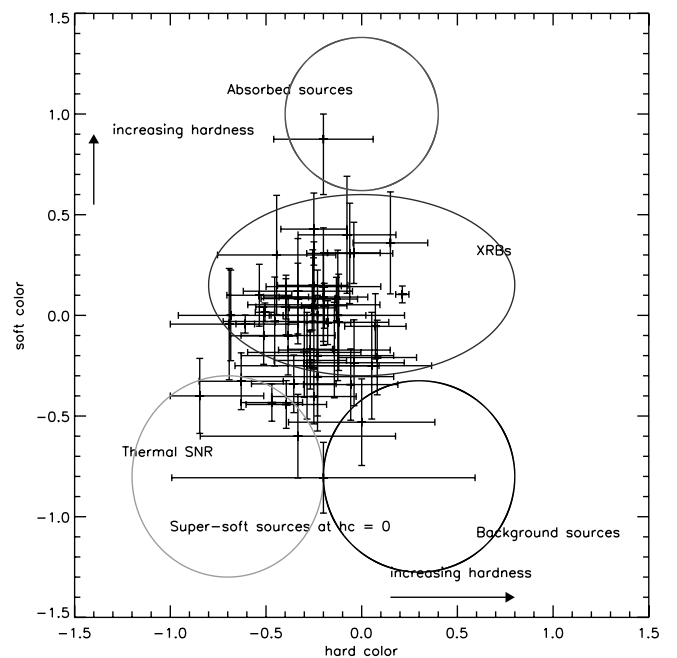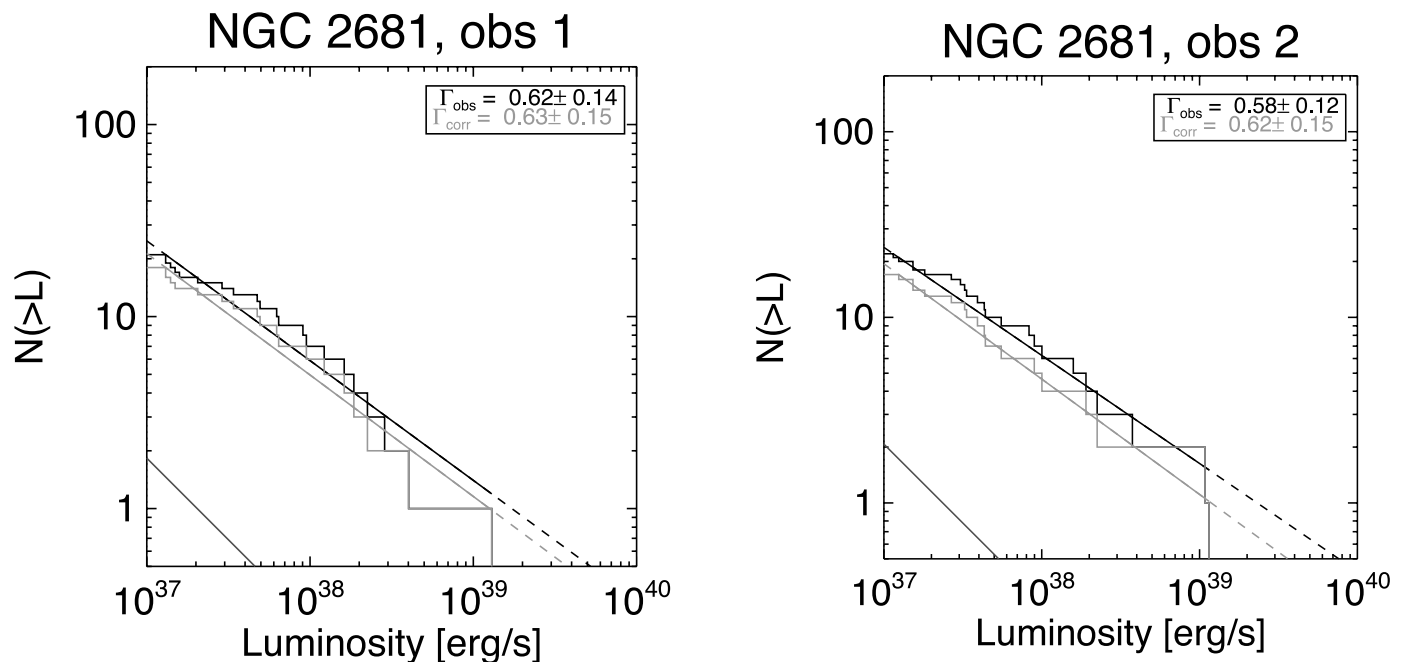
Fig. 16.—Cumulative luminosity function of the X-ray point sources in NGC 2681. [*See the electronic edition of the Journal for a color version of this figure.*]

This background calculation provides a number N of sources that are projected along the slope of the *Chandra* Deep Field $\log(N) - \log(S)$. These N sources are then subtracted from the data LF using a nearest neighbor matching routine; hence, the source with luminosity that is closest to the random background luminosity is removed. Thus, the red curves in the plots (see, e.g., Fig. 2) provide the ideal theoretical background LF given the spatial region sampled and the duration of the observation. The difference between the subtracted sources and the red curve is due to Poisson random deviation in the simulation of the background LF. The goodness-of-fit estimate is performed by simulating a luminosity distribution with the best-fit slope. One million iterations are performed and the mean slope and mean deviation of the simulated luminosity distributions are found. The goodness-of-fit estimate comes from Crawford et al. (1970) and is defined as

$$\sigma_{MC}^2/\sigma^2,$$

where σ_{MC} is the mean deviation of the simulated LFs and σ is the observed deviation, as defined in Crawford et al. (1970, eq. [13]). If the data are well fitted by a single, unbroken power-law distribution, then the goodness-of-fit value should approach 1. It should be noted that, for several of the galaxies, the exposure times of the separate observations are quite different and, thus, the detection thresholds are also different. As such, the range of luminosities fitted will be different for those galaxies. For example, in the case of M101, the luminosity thresholds are 4.4×10^{36} and 4.6×10^{37} ergs s^{-1} for the 100 and 10 ks observations, respectively; the best-fit slopes are 0.69 and 1.70, respectively; and the goodness-of-fit values are 1.60 and 1.06, respectively. The fit to the shorter data set is much steeper, but also a better fit, suggesting that the high-luminosity end of the LF may be better fitted with a steeper component or a high-luminosity cutoff.

In the catalog table for each galaxy, we also present variability information for each source. This includes both long-term variability (statistically significant variability between each observa-

tion) and short-term, statistically significant variability during each observation.

2.3. *Optical Data Analysis*

Except where noted, all optical observations were obtained with the Fred L. Whipple Observatory 48 inch (1.2 m) telescope located at Mount Hopkins, Arizona. Data were obtained during two observing runs, 2001 February 19–21 and 2001 December 15–16. Filters used were *U, B, V, R, I*, and wide Hα and S II. Observations of M83 were obtained using the Southeastern Association for Research in Astronomy (SARA) 0.9 m telescope at Kitt Peak National Observatory, Arizona. Data were obtained on 2001 May 29 using V, Hα, and Hα continuum filters. Data were reduced in the standard fashion using IRAF version 2.12 and the MSCRED package, used for analysis of data taken with the 4-shooter CCD on the FLWO 48 inch (1.2 m) telescope. Astrometric alignment of images was performed using the WCSTools software from the SAO Telescope Data Center using objects identified in both X-ray and optical observations as either foreground stars or background AGNs, as identified in SIMBAD catalog queries. For the galaxies NGC 1291 and IC 5332, which are located in the southern hemisphere, we utilized data from the Digitized Sky Survey and no further registration was performed. None of the optical data were taken simultaneously with the X-ray, but all data were obtained within a year of the X-ray observations. For the FLWO and SARA data, resolution is determined by atmospheric stability from the sites in Arizona. Typical observations have 2″ seeing. All optical images presented here are *V* band unless otherwise noted. A more detailed analysis of the optical data will be presented in a future paper.

3. NOTES ON INDIVIDUAL GALAXIES

3.1. *NGC 278, Sb*

At just over 2′ in diameter, NGC 278 is the least extended galaxy in our sample (see Fig. 4). As can be seen in Figure 5, the X-ray emission consists of around 15 point sources embedded in extensive unresolved emission. The completeness limit for
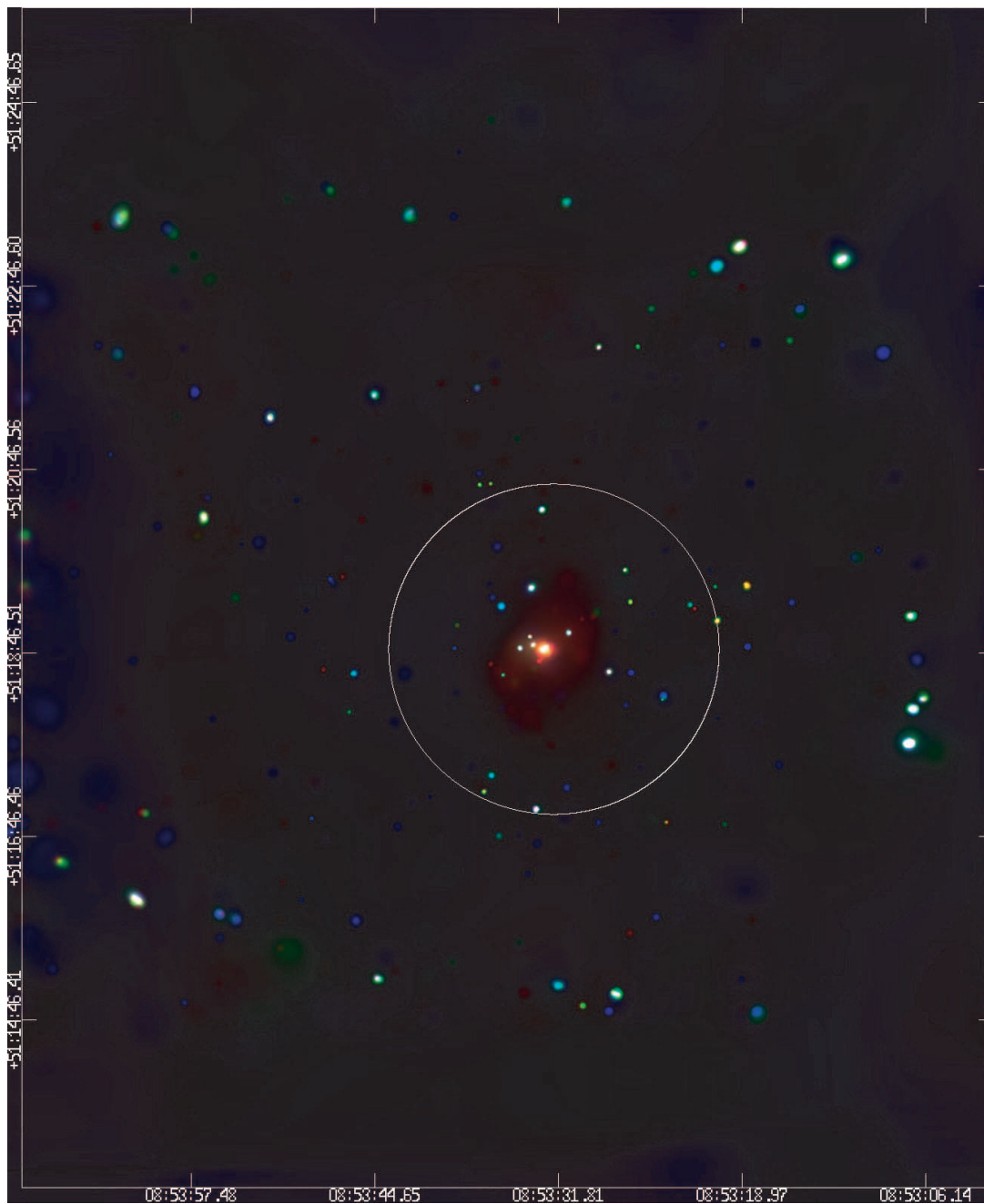
Fig. 17.—Merged *Chandra* observation of NGC 2681. Adaptively smoothed. Red is 0.3–1 keV, green 1–2 keV, and blue 2–8 keV.
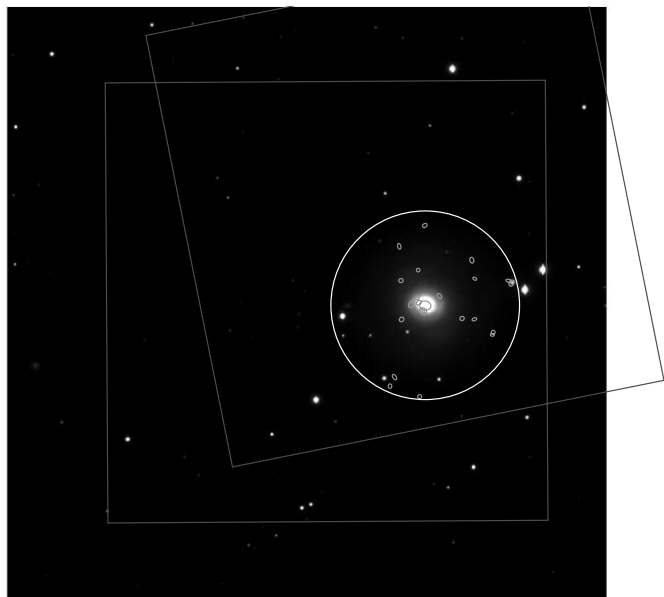
Fig. 18.—FLWO optical image of NGC 2681 with *Chandra* sources overlaid. The white circle is the D25 extent of the galaxy. The scale of the image is $10' \times 10'$. [*See the electronic edition of the Journal for a color version of this figure.*]

Fig. 19.—Color-color diagram of the X-ray point sources in NGC 2681.

each observation is 3.7×10^{37} ergs s^{-1}. Though some of this emission is likely due to point source confusion, the ability of *Chandra* to resolve point sources in galaxies of similar distance in a similar exposure time (e.g., M74, see § 3.2) implies that either (1) much of the unresolved emission is due to hot gas and not faint point sources or (2) the shape of the LF of NGC 278 is drastically different from other more nearby galaxies (e.g., M31), which show an LF turnover at lower luminosities (Shirey et al. 2001). Though the Galactic n_H in the direction of NGC 278 (1.29×10^{21} cm^{-2}) is the highest in our sample, it is still relatively low and should not hamper the detection of faint sources.

Plotted in Figure 4 is the cumulative point source luminosity function for both *Chandra* observations of NGC 278 with best-fit single power-law slopes. Though the relatively steep slopes
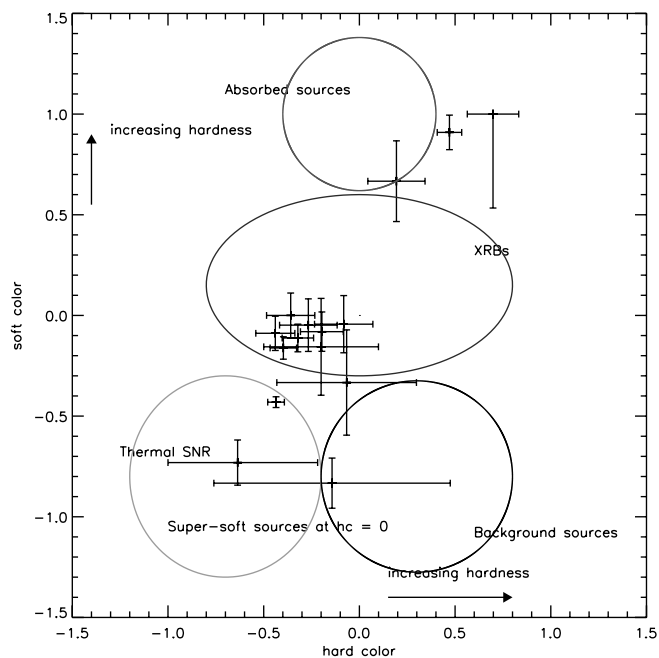
indicate an evolved stellar population, since there are only 14 point sources, the parameters of the luminosity function (LF) cannot be accurately determined. Figure 6 shows an optical image of NGC 278 with the X-ray point sources marked. Following the method of Prestwich et al. (2003) for source classification by X-ray colors, the population appears to be dominated by low-mass X-ray binaries (LMXBs) with evidence for high absorption (see Fig. 7). 20% of the sources exhibit statistically significant variability between the two *Chandra* observations at the 90% level.

3.2. *M74 (NGC 628), Sc*

M74 has been observed twice with *Chandra* and twice with *XMM-Newton*. The first *XMM-Newton* observation was performed as a target-of-opportunity (TOO) observation to observe
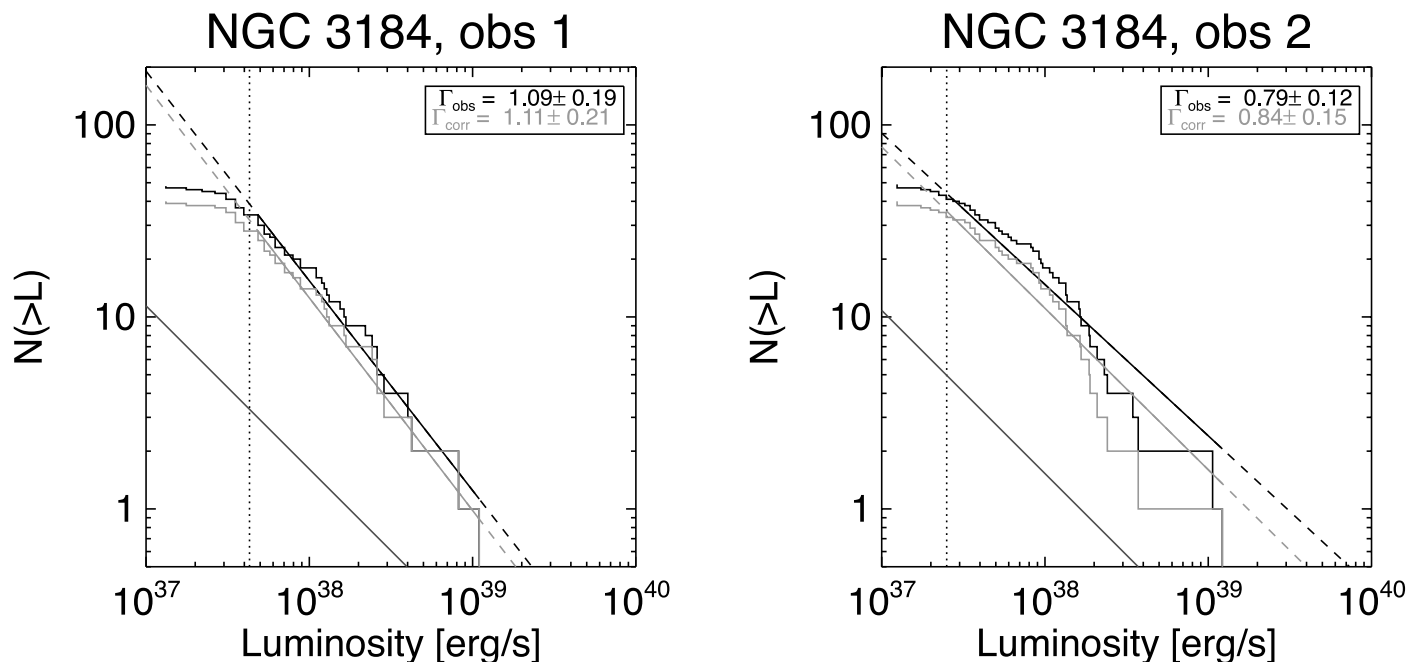

Fig. 20.—Cumulative luminosity function of the X-ray point sources in NGC 3184. [*See the electronic edition of the Journal for a color version of this figure.*]
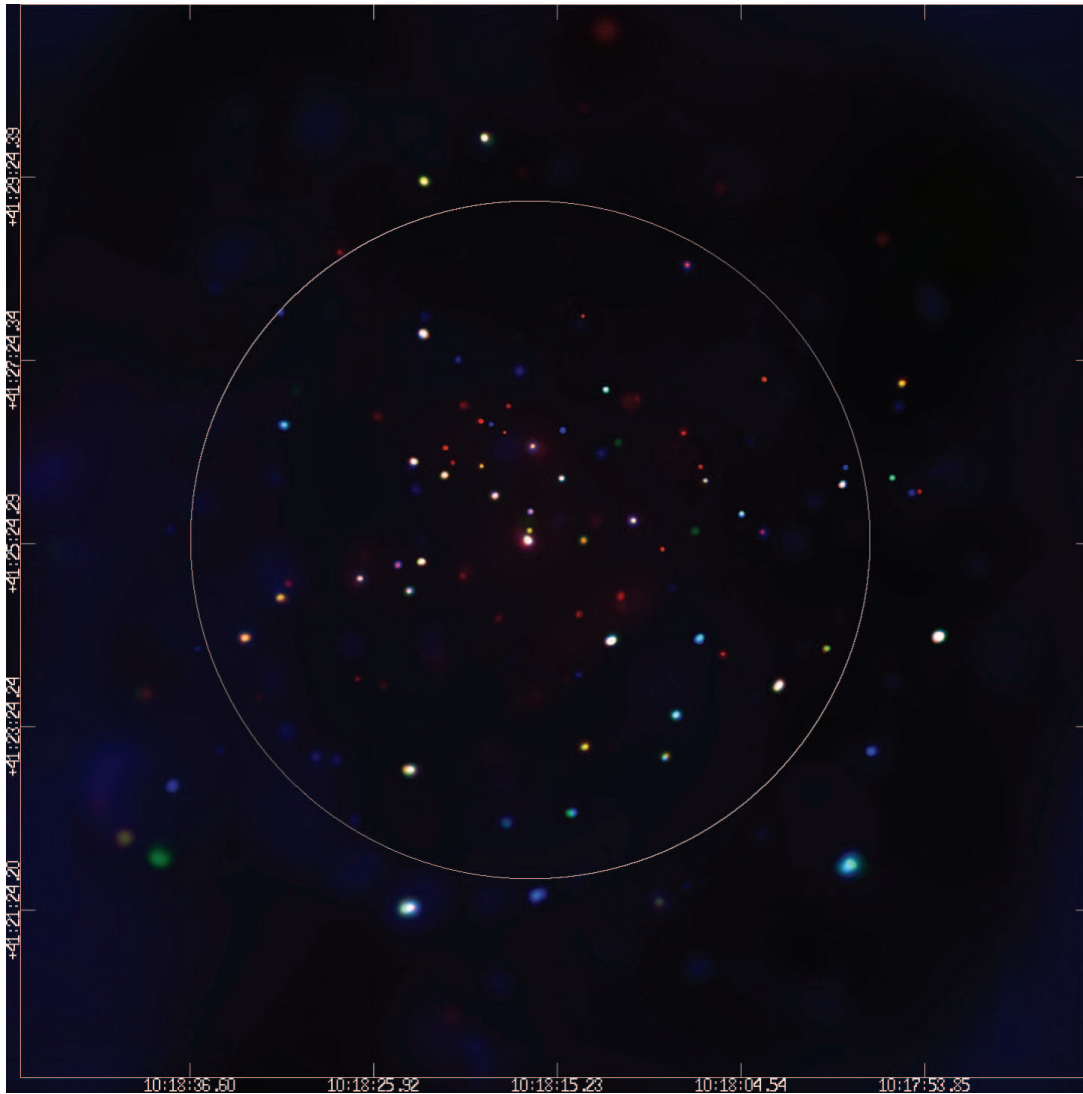
Fig. 21.—Merged *Chandra* observation of NGC 3184. Adaptively smoothed. Red is 0.3–1 keV, green 1–2 keV, and blue 2–8 keV.

a recent supernova in M74, SN2002ap. A detailed study of those data is presented in Soria & Kong (2002). The emission is dominated by 67 point sources with little evidence of unresolved emission. At only 8.8 Mpc, the Sc spiral M74 offers one of the best comparisons to the Milky Way in our sample.

The most interesting aspect of the M74 observations is the ultraluminous source CXOU J013651.1+154547, which is discussed in detail in Krauss et al. (2005). This remarkable source exhibits quasi-periodic flaring and changes in spectral state, suggesting that it is likely a microquasar similar to the Galactic microquasar GRS 1915+105.

The LF slope of M74 is relatively steep (1.16) as compared with star-forming galaxies, indicating that the X-ray source population is dominated by LMXBs. The completeness limit for each observation is 1.6×10^{37} ergs s^{-1}. The X-ray colors indicate a mix of high- and low-mass binaries with a few possible supernova remnants (SNRs). There is no radial dependence of the source colors, indicating no clear separation of bulge and disk sources. 23% of the sources exhibit long-term variability. Plotted in Figures 8, 9, 10, and 11 are the LF, smoothed three-color X-ray image, optical image with X-ray source overlays, and X-ray color-color diagram.

3.3. *NGC 1291, S0/a*

NGC 1291 is one of the best examples of an X-ray–bright S0 galaxy in the local universe. It has been observed twice with *Chandra* with results presented in Irwin et al. (2002). We build on their work by extending the source catalog from 48 to 93 discrete sources. Note the relatively steep luminosity function in Figure 12, which is characteristic of early-type galaxies (Sarazin et al. 2000). The X-ray colors indicate a population dominated by LMXBs. There is clear evidence of spiral structure in the unresolved X-ray emission that is not evident in optical images. 29% of the sources exhibit long-term variability. Plotted in Figures 12, 13, 14, and 15 are the LF, smoothed three-color X-ray image, optical image with X-ray source overlays, and X-ray color-color diagram. The completeness limits for the two observations are 1.8×10^{37} and 2.9×10^{37} ergs s^{-1}.

3.4. *NGC 2681, S0/a*

NGC 2681 is an early-type galaxy with evidence for a barlike structure present in the unresolved X-ray emission. The colors indicate an LMXB population. 43% of the X-ray source population (10 of 23 sources) exhibits long-term variability. Plotted
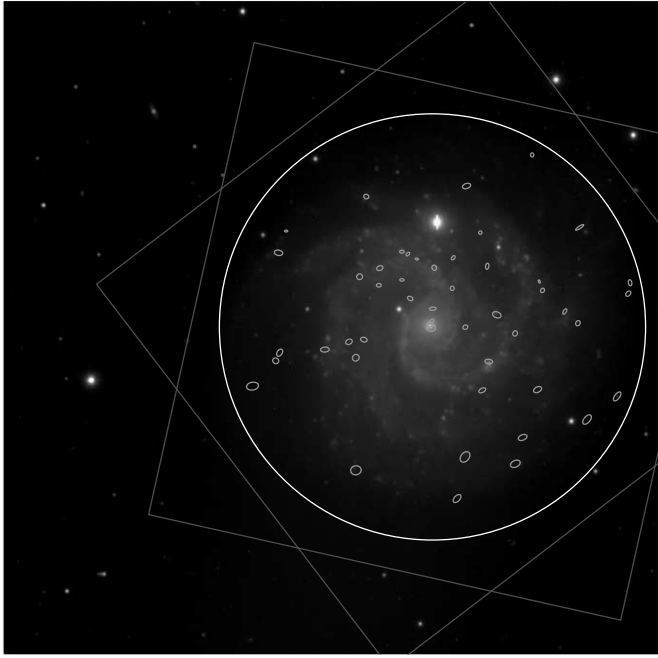
FIG. 22.—FLWO optical image of NGC 3184 with *Chandra* sources overlaid. The white circle is the D25 extent of the galaxy. The scale of the image is $10' \times 10'$. [*See the electronic edition of the Journal for a color version of this figure.*]
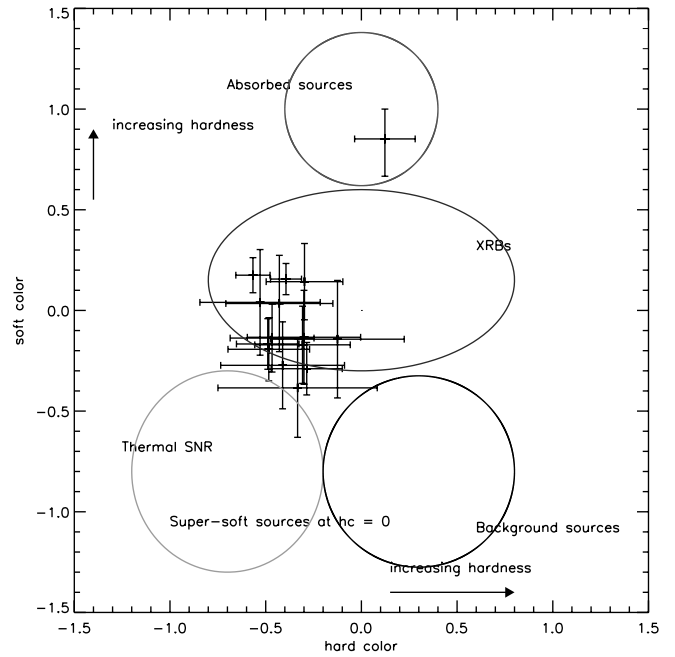

FIG. 23.—Color-color diagram of the X-ray point sources in NGC 3184. [*See the electronic edition of the Journal for a color version of this figure.*]

in Figures 16, 17, 18, and 19 are the LF, smoothed three-color X-ray image, optical image with X-ray source overlays, and X-ray color-color diagram. The completeness limit for each observation is 1.0×10^{37} ergs s^{-1}.

3.5. *NGC 3184, Scd*

NGC 3184 was observed twice with *Chandra*, the second time as a TOO observation to observe a recent supernova, SN 1999gi (Schlegel 2001). The LF is less steep than the early-type spirals NGC 1291 and NGC 2681, though still not as flat as the actively star-forming M83 (3.9). The X-ray colors show a mix

of low- and high-mass binaries and SNRs. There is a slight enhancement in the unresolved emission toward the southwest, coincident with the optical spiral arm in that direction. 24% of the population exhibits long-term variability. Plotted in Figures 20, 21, 22, and 23 are the LF, smoothed three-color X-ray image, optical image with X-ray source overlays, and X-ray color-color diagram. The completeness limits for the two observations are 4.3×10^{37} and 2.5×10^{37} ergs s^{-1}.

3.6. *NGC 4314, SBa*

NGC 4314 is a bright SB galaxy with a ring of circumnuclear star formation. Unresolved emission in the star-forming region dominates the emission, with only 22 point sources detected.
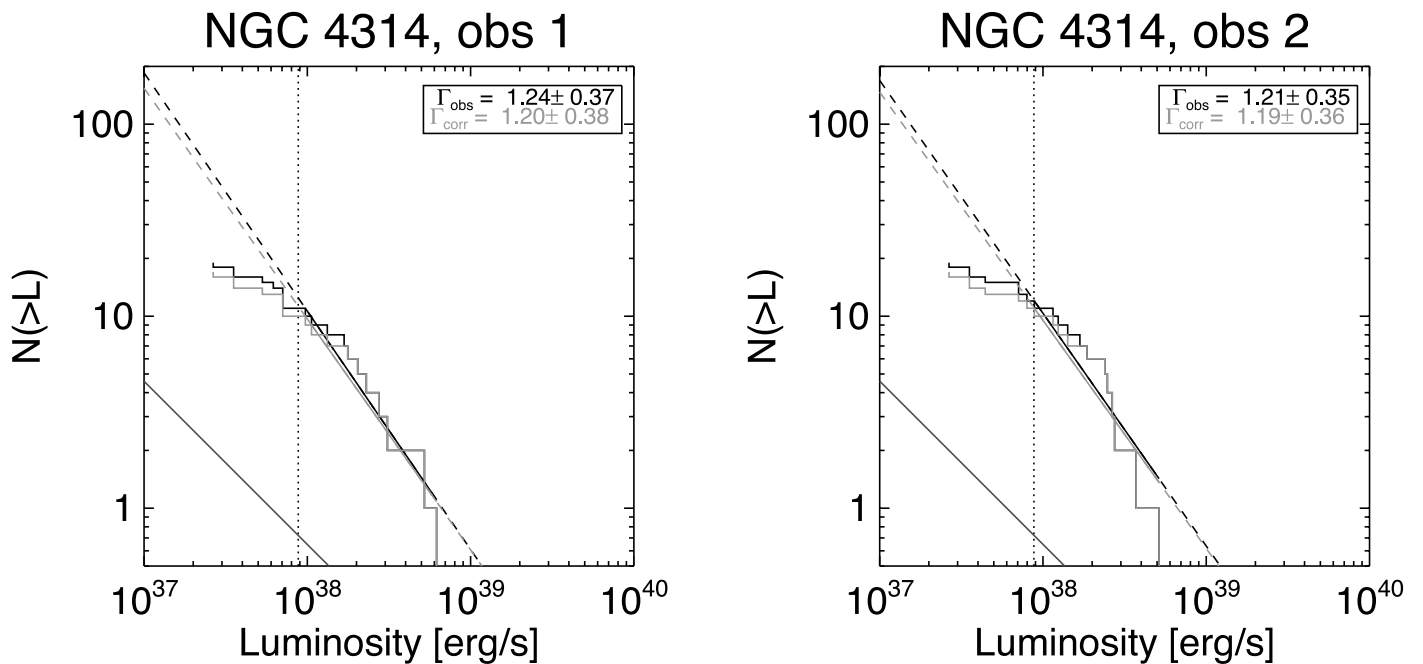

FIG. 24.—Cumulative luminosity function of the X-ray point sources in NGC 4314. [*See the electronic edition of the Journal for a color version of this figure.*]
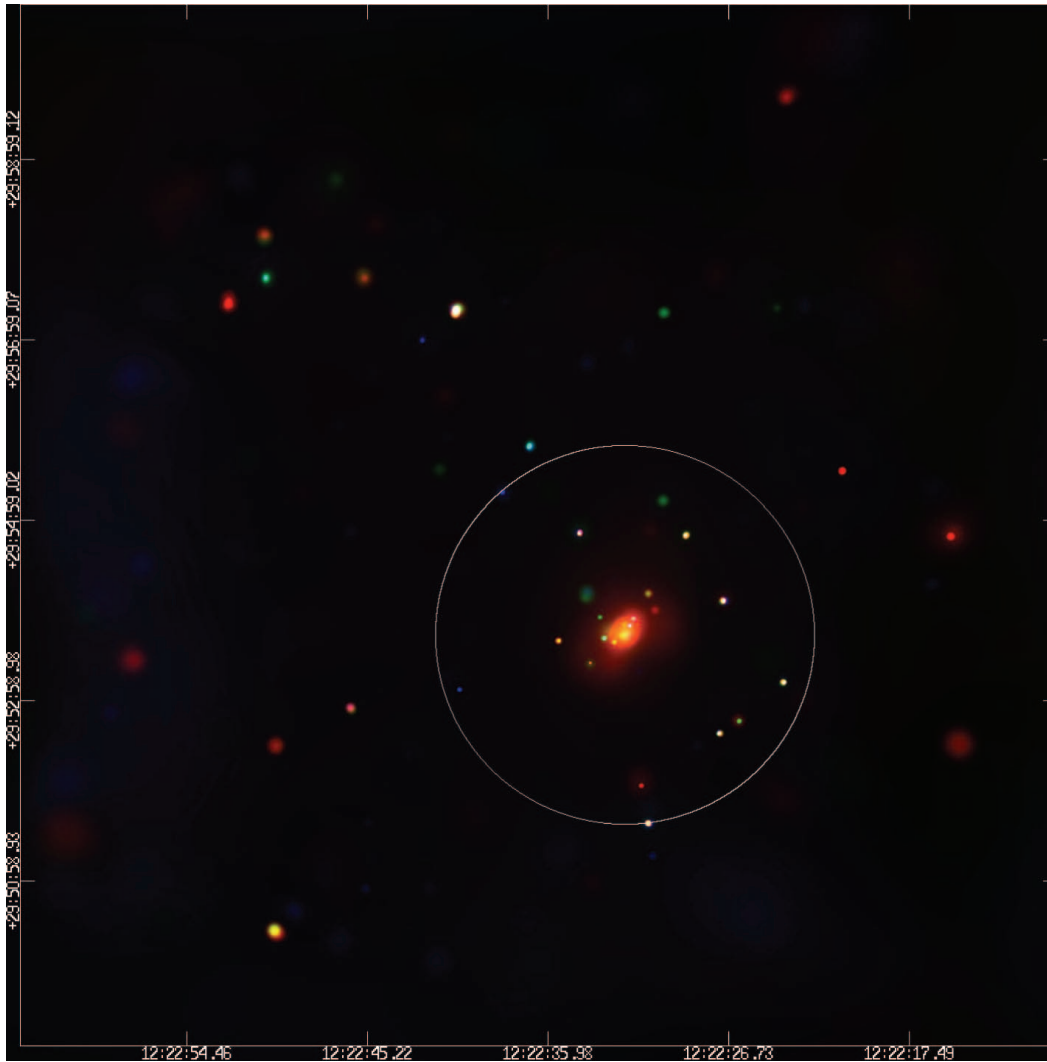
Fig. 25.—Merged *Chandra* observation of NGC 4314. Adaptively smoothed. Red is 0.3–1 keV, green 1–2 keV, and blue 2–8 keV.
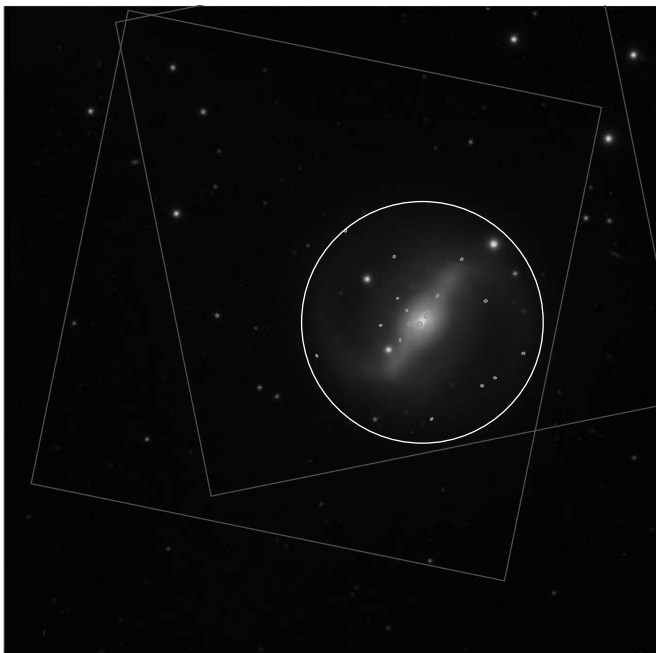

Fig. 26.—FLWO optical image of NGC 4314 with *Chandra* sources overlaid. The white circle is the D25 extent of the galaxy. The scale of the image is $10' \times 10'$. [*See the electronic edition of the Journal for a color version of this figure.*]
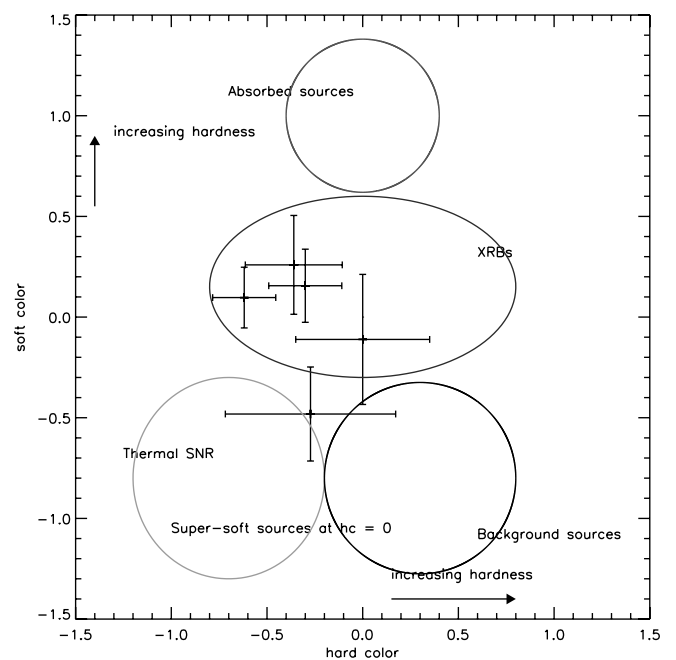

Fig. 27.—Color-color diagram of the X-ray point sources in NGC 4314. [*See the electronic edition of the Journal for a color version of this figure.*]
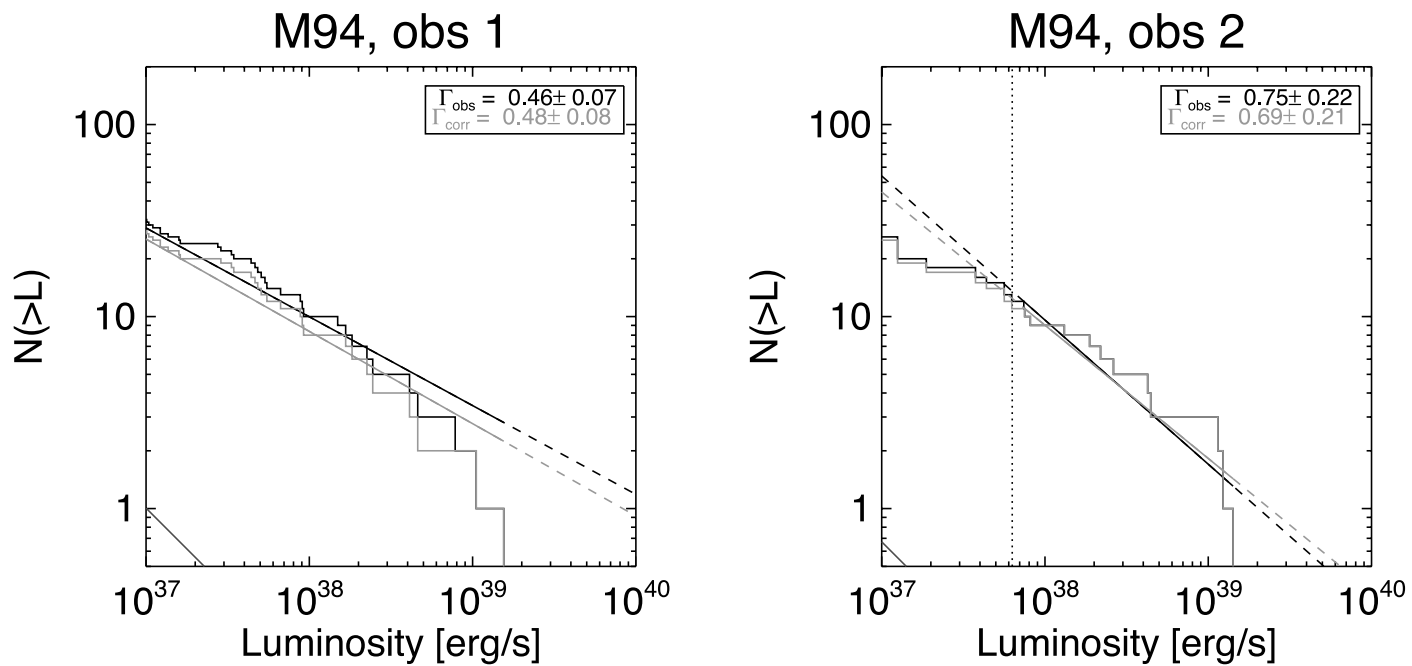
FIG. 28.—Cumulative luminosity function of the X-ray point sources in M94. Note that the observations cover only the nuclear region of the galaxy and, as such, the LF should be considered indicative of the star-forming nuclear region and not the galaxy as a whole. [*See the electronic edition of the Journal for a color version of this figure.*]
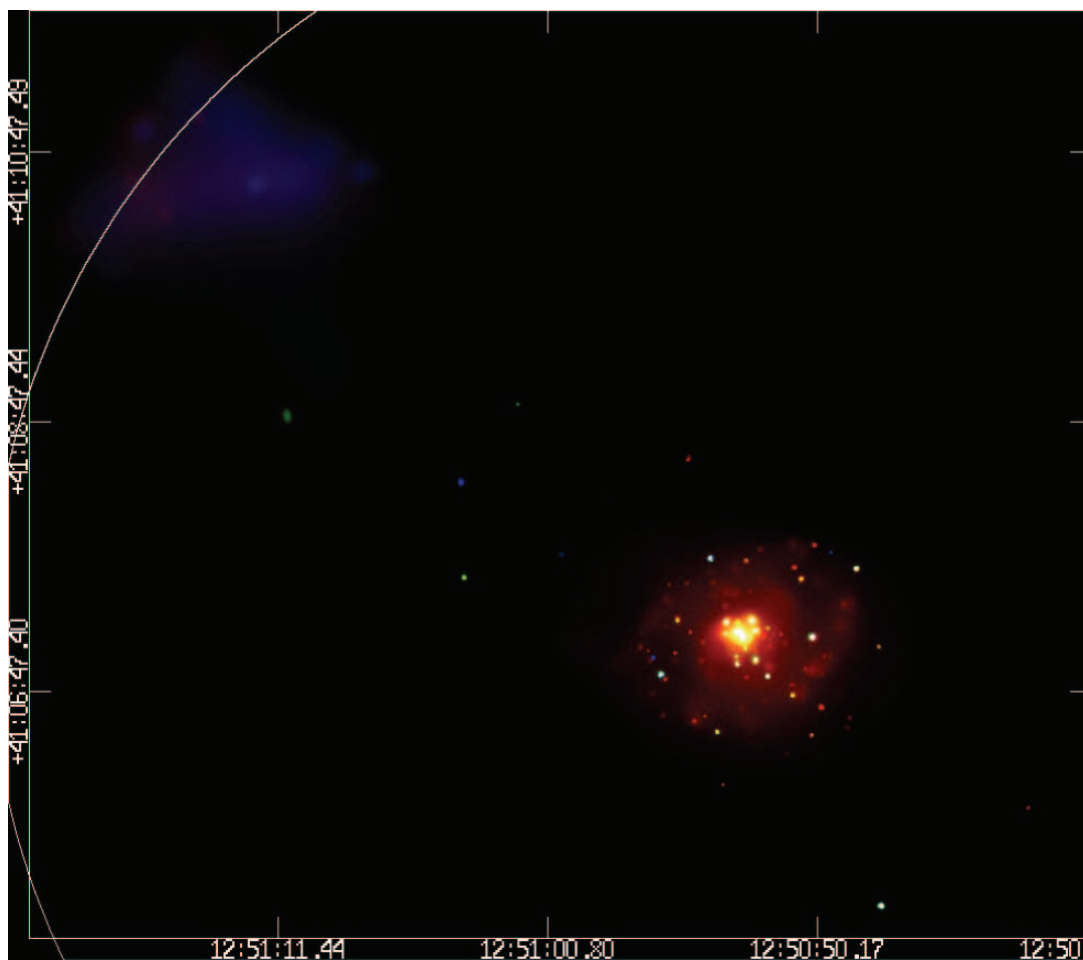

FIG. 29.—Merged *Chandra* observation of M94. Adaptively smoothed. Red is 0.3−1 keV, green 1−2 keV, and blue 2−8 keV.
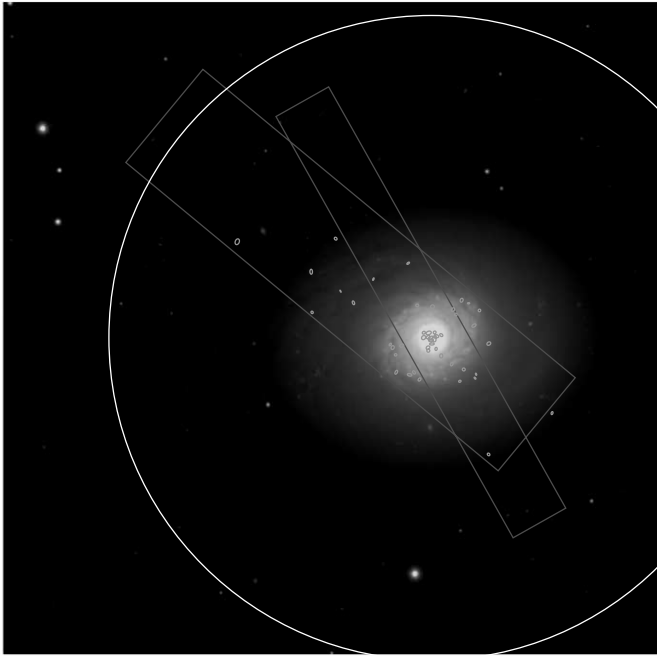
FIG. 30.—FLWO optical image of M94 with *Chandra* sources overlaid. The white circle is the D25 extent of the galaxy. The red boxes show the locations of the ACIS-S3 subarray during the two *Chandra* observations (the wider box is the longer observation). The scale of the image is $10' \times 10'$. [*See the electronic edition of the Journal for a color version of this figure.*]
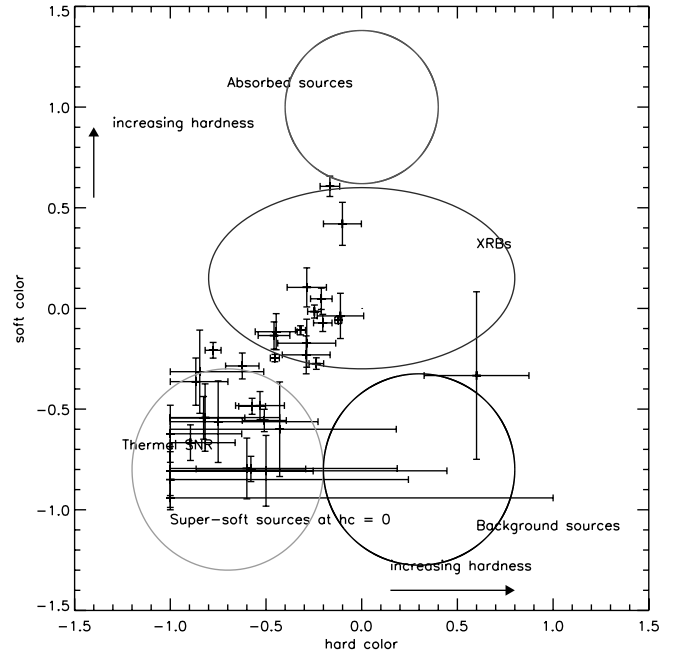

FIG. 31.—Color-color diagram of the X-ray point sources in M94. Again note that the observation only covers the nuclear region and thus this plot only represents those sources in that region. [*See the electronic edition of the Journal for a color version of this figure.*]

NGC 4314 has been studied extensively with *HST* (see Benedict et al. 1992 and subsequent paper) showing clear evidence for star formation in a circumnuclear ring. We detect enhanced unresolved X-ray emission coincident with this ring.

The X-ray colors indicate an LMXB dominated population, though insufficient exposure time prevents the detection of faint ($L_X < 10^{37}$ ergs s^{-1}) potential SNRs in the nuclear starburst region. The LF slope is fairly flat, though the low number of sources prevents the parameters of the LF fit from being precisely determined. 14% of the population exhibits long-term

variability. Plotted in Figures 24, 25, 26, and 27 are the LF, smoothed three-color X-ray image, optical image with X-ray source overlays, and X-ray color-color diagram. The completeness limit for each observation is 8.8×10^{37} ergs s^{-1}.

3.7. *M94 (NGC 4736), Sab*

M94 has several bright nuclear sources, none of which is clearly an AGN. The observation was performed with a 1/4 subarray (reducing the frame time from 3.2 to 0.84 s) in order to mitigate the effects of pile-up on the count rates and spectra of the nucleus and other bright sources. As such, we only observe
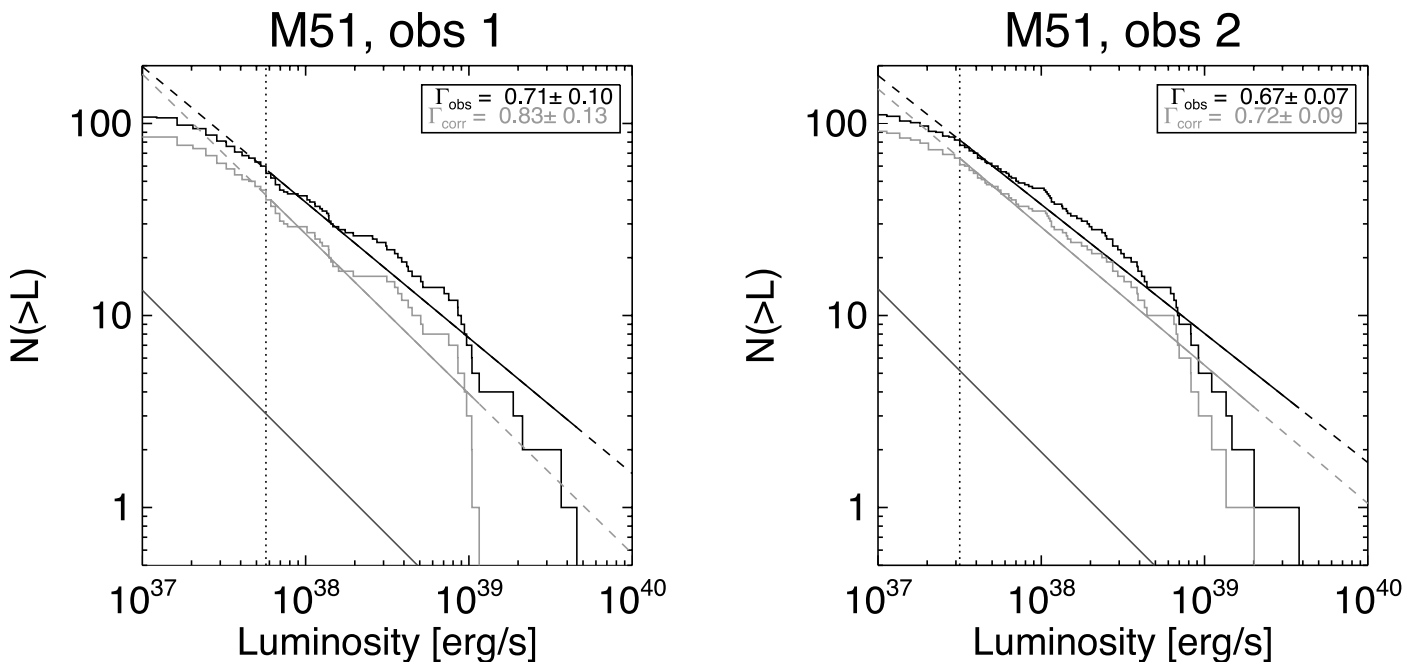

FIG. 32.—Cumulative luminosity function of the X-ray point sources in M51. [*See the electronic edition of the Journal for a color version of this figure.*]
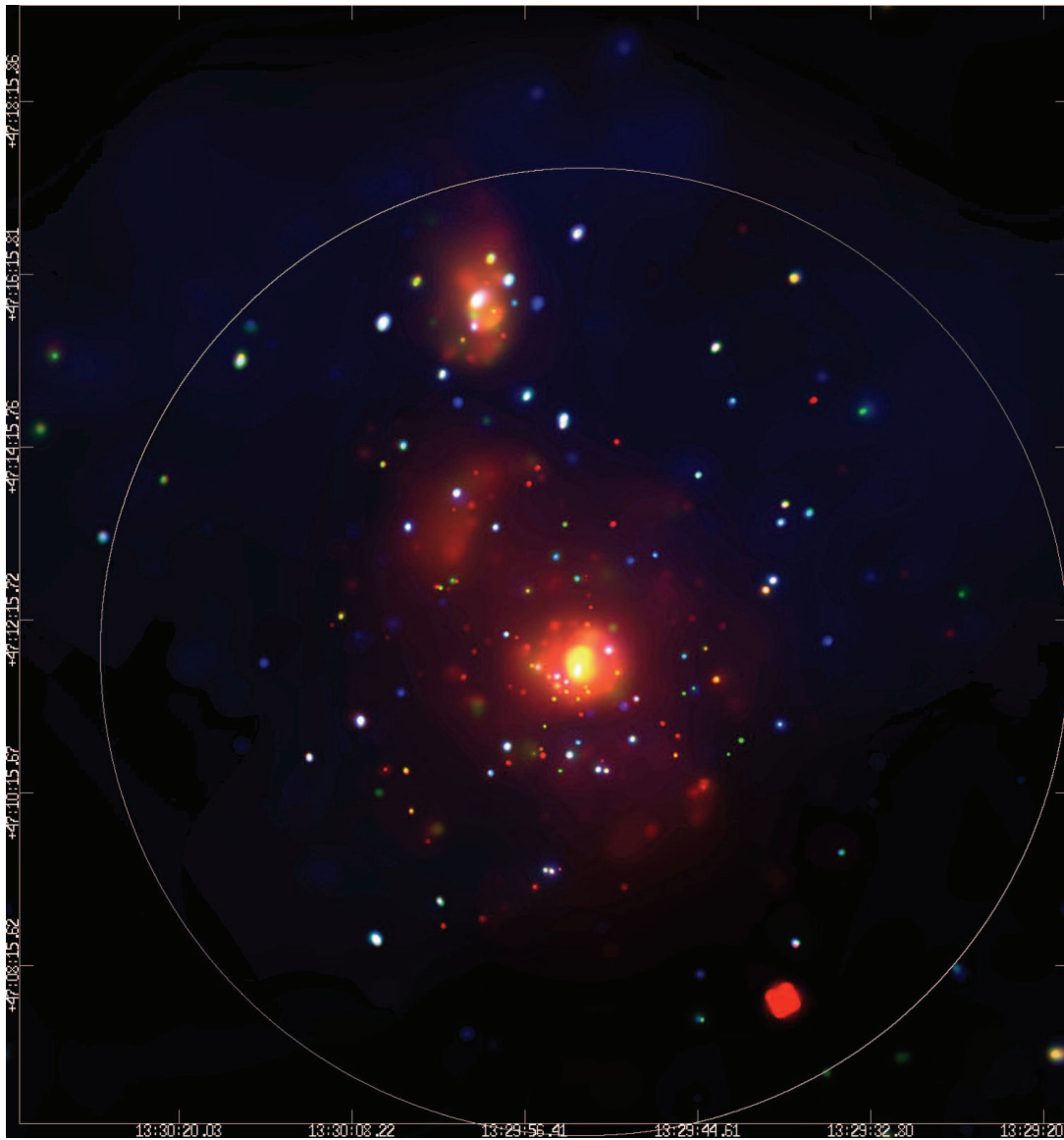
F_{IG}. 33.—Merged *Chandra* observation of M51. Adaptively smoothed. Red is 0.3–1 keV, green 1–2 keV, and blue 2–8 keV.
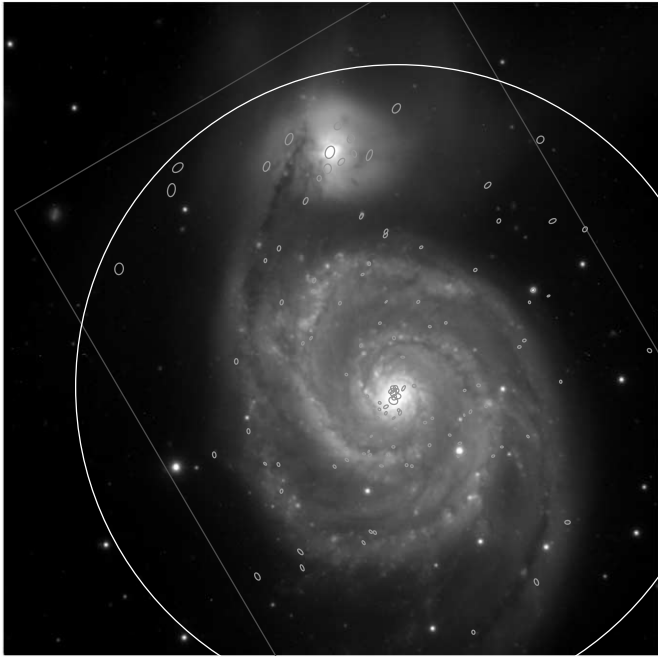
Fig. 34.—FLWO optical image of M51 with *Chandra* sources overlaid. The white circle is the D25 extent of the galaxy. The scale of the image is $10' \times 10'$. [*See the electronic edition of the Journal for a color version of this figure.*]
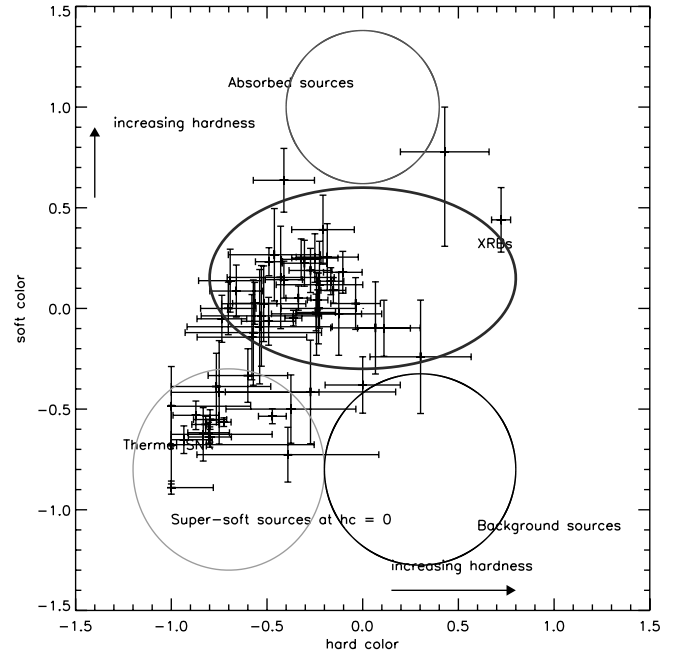

Fig. 35.—Color-color diagram of the X-ray point sources in M51. [*See the electronic edition of the Journal for a color version of this figure.*]

a slice $2' \times 8'$ of the galaxy and the luminosity functions should therefore be taken as indicative of the nuclear region rather than the full galaxy. An analysis of the longer (47 ks) M94 observation is presented in Eracleous et al. (2002), and we extend their analysis to include a short (2 ks) observation and catalog an additional 16 point sources.

The LF of M94 is quite flat, and the X-ray source population is dominated by potential SNRs and X-ray binaries (XRBs). This implies a high star formation rate in the nucleus, in agreement with Hα and radio measurements (Pogge 1989; Turner &

Ho 1994). This can be contrasted with the nucleus of M31, where the LF slope is quite steep, indicating a population dominated by LMXBs (Kong et al. 2003). The spiral nucleus shows clear unresolved emission tracing the spiral arms. 14% of the sources exhibit long-term variability, though this should be considered an extreme lower limit as the first observation was around 20 times the duration of the second. Plotted in Figures 28, 29, 30, and 31 are the LF, smoothed three-color X-ray image, optical image with X-ray source overlays, and X-ray color-color diagram. The completeness limits for the two observations are 3.1×10^{36} and 6.3×10^{37} ergs s^{-1}.

Fig. 36.—Cumulative luminosity function of the X-ray point sources in M83. [*See the electronic edition of the Journal for a color version of this figure.*]

Fig. 37.—Merged *Chandra* observation of M83. Adaptively smoothed. Red is 0.3–1 keV, green 1–2 keV, and blue 2–8 keV.

Fig. 38.—SARA optical image of M83 with *Chandra* sources overlaid. The white circle is the D25 extent of the galaxy. The scale of the image is 6′ × 6′. [*See the electronic edition of the Journal for a color version of this figure.*]

Fig. 39.—Color-color diagram of the X-ray point sources in M83. [*See the electronic edition of the Journal for a color version of this figure.*]

M101, obs 1

$\Gamma_{obs} = 0.52 \pm 0.04$
$\Gamma_{corr} = 0.55 \pm 0.04$

M101, obs 2

$\Gamma_{obs} = 0.78 \pm 0.13$
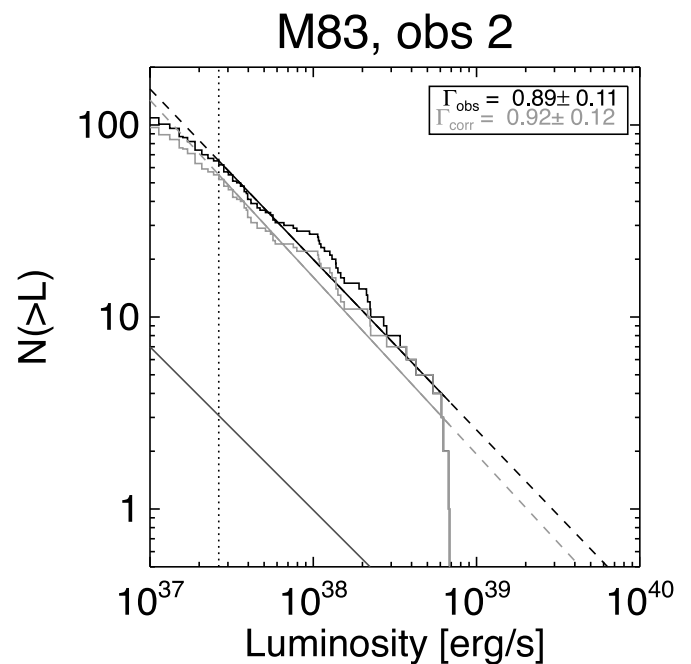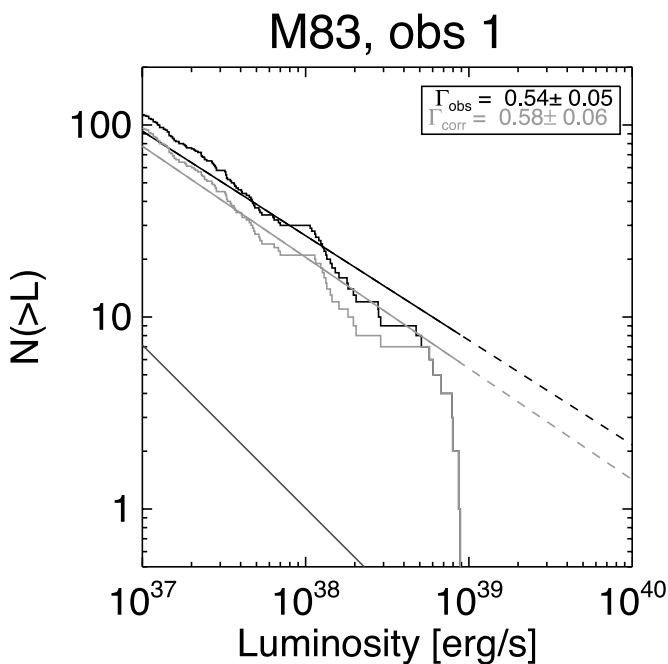$\Gamma_{corr} = 0.73 \pm 0.15$

FIG. 40.—Cumulative luminosity function of the X-ray point sources in M101. [*See the electronic edition of the Journal for a color version of this figure.*]
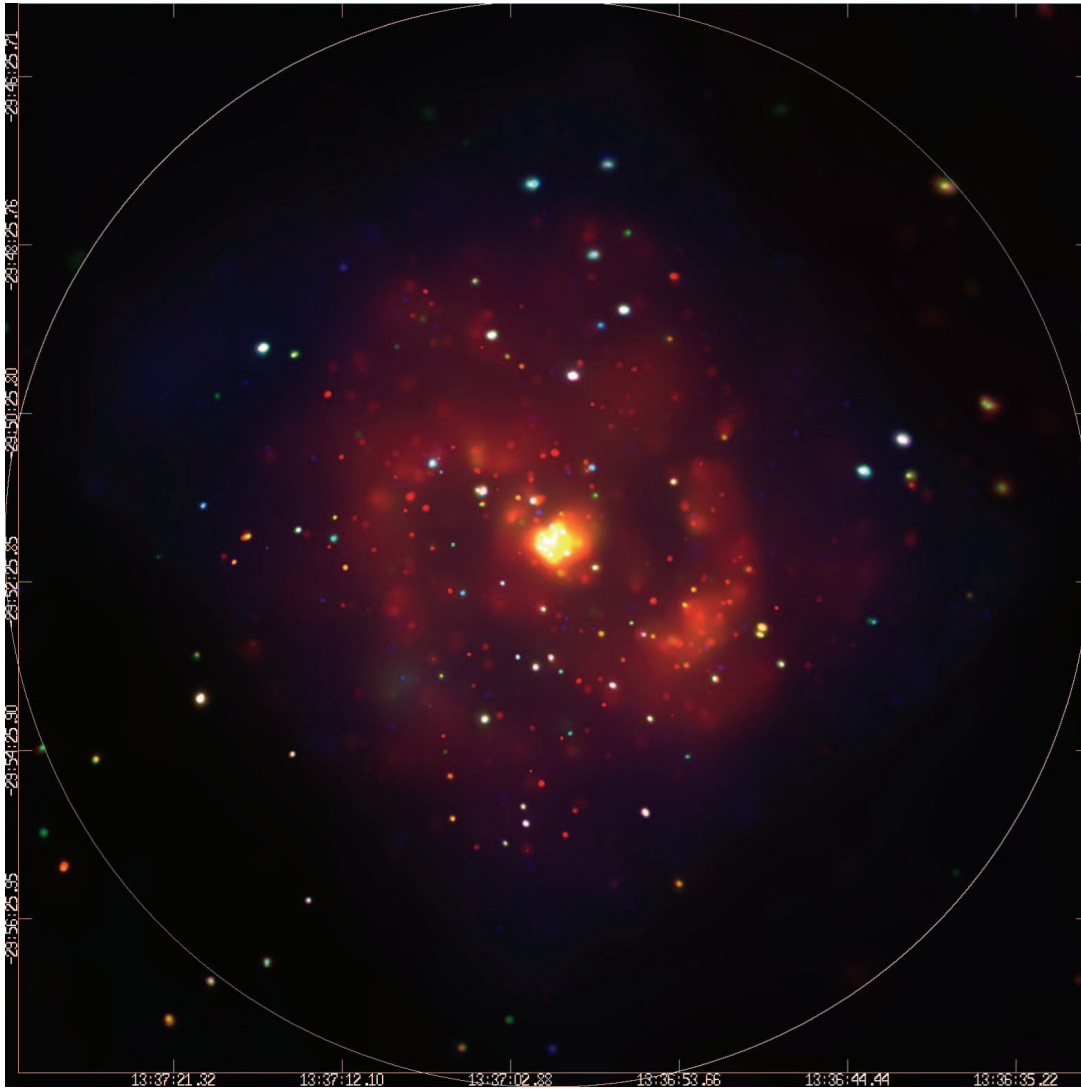

FIG. 41.—Merged *Chandra* observation of M101. Adaptively smoothed. Red is 0.3–1 keV, green 1–2 keV, and blue 2–8 keV.
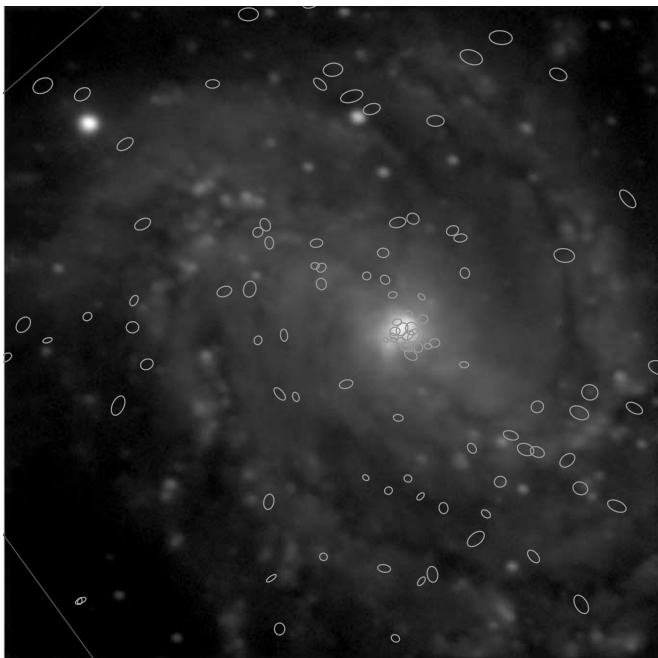
Fig. 42.—DSS optical image of M101 with *Chandra* sources overlaid. The white circle is the D25 extent of the galaxy. The scale of the image is $30' \times 30'$. [*See the electronic edition of the Journal for a color version of this figure.*]
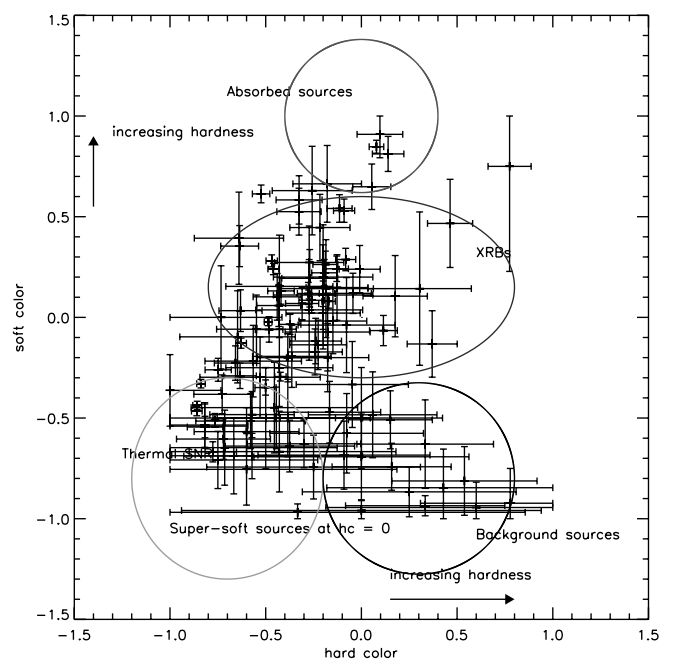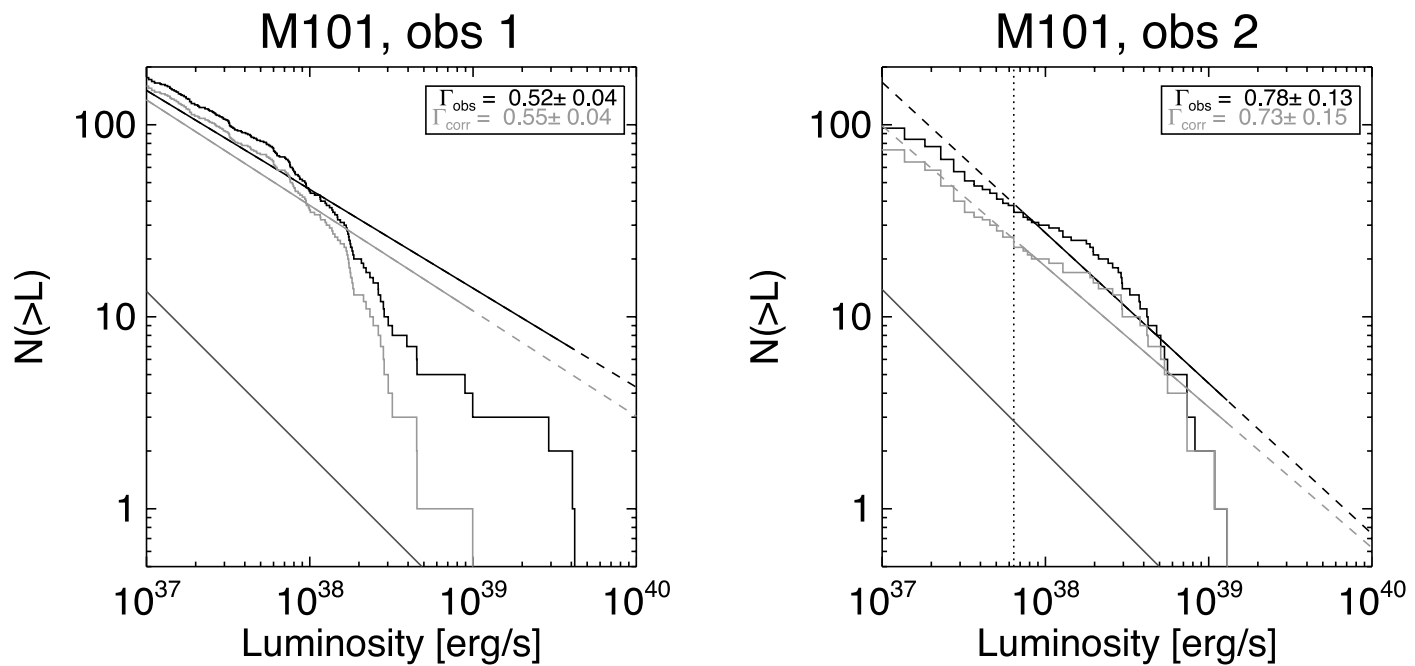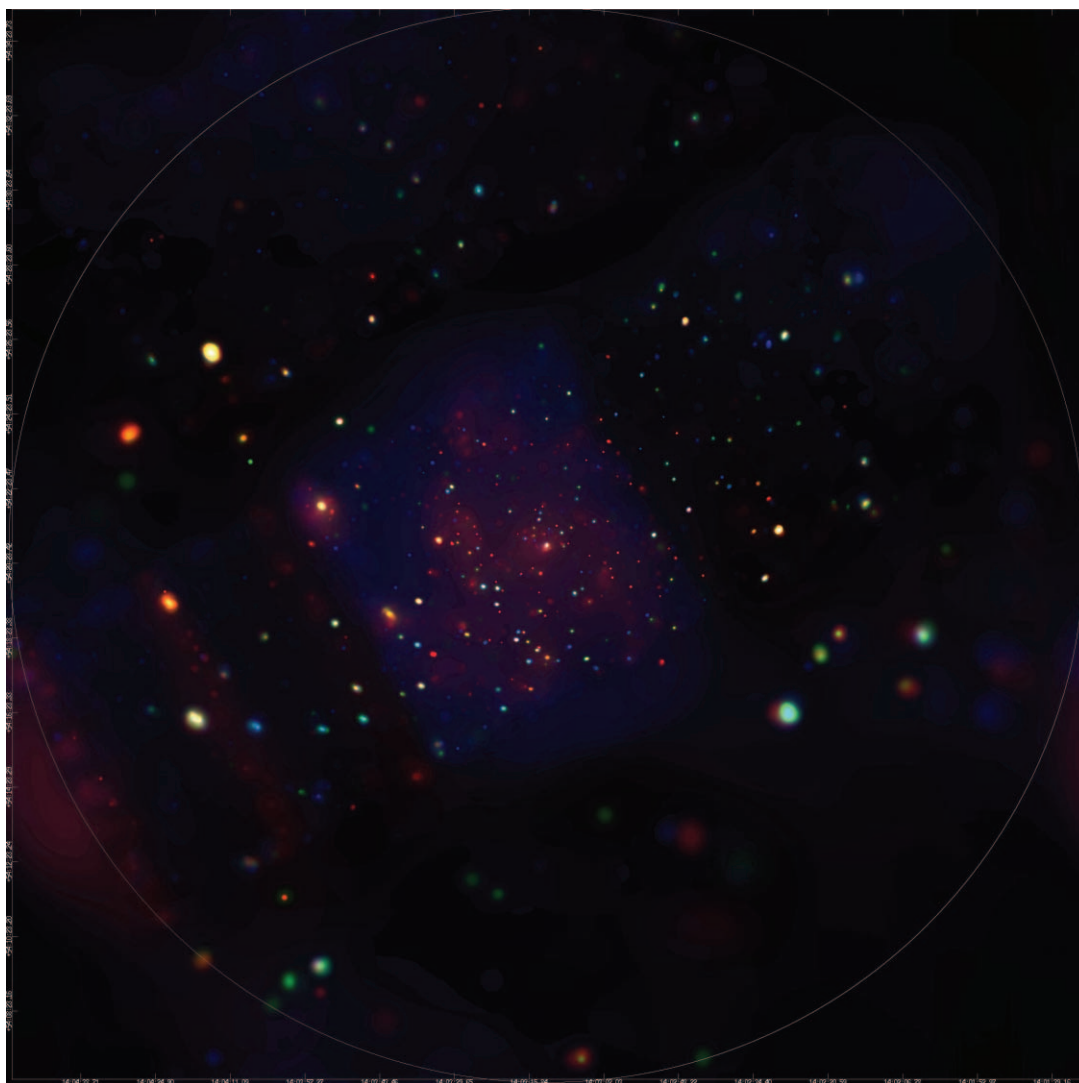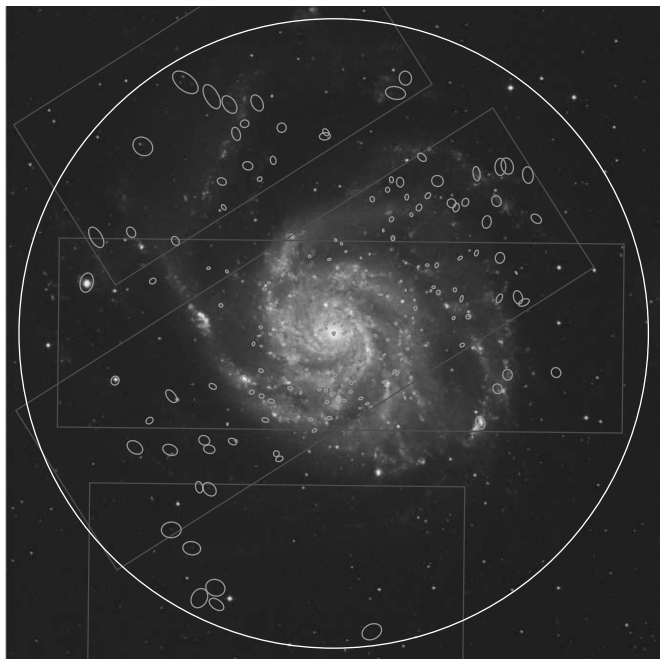

Fig. 43.—Color-color diagram of the X-ray point sources in M101. [*See the electronic edition of the Journal for a color version of this figure.*]

3.8. *M51 (NGC 5194/95), Sbc*

At just over 6 Mpc, M51 is the closest example of a face-on interacting galaxy pair. It contains a wealth of point sources and unresolved emission clearly tracing the spiral arms in both galaxies. There are four ULXs. A detailed analysis of M51 is presented in Terashima & Wilson (2003). We extend their catalog by an additional 15 sources and include sources on the ACIS S2 chip.

The LF slope is also quite flat (almost as flat as the LFs of starburst galaxies; Kilgard et al. 2002) and the X-ray colors indicate a mix of SNRs and low- and high-mass binaries, as well as some supersoft sources (SSSs). 31% of the sources exhibit long-term variability. Plotted in Figures 32, 33, 34, and 35 are the LF, smoothed three-color X-ray image, optical image with X-ray source overlays, and X-ray color-color diagram. The S3 completeness limits for the two observations are 4.1×10^{37} and 2.2×10^{37} ergs s^{-1}. The FI chip completeness limits for the two observations are 5.7×10^{37} and 3.2×10^{37} ergs s^{-1}.

3.9. *M83 (NGC 5236), Sc*

The X-ray observations of M83 consist of many bright point sources and unresolved emission tracing the spiral arms. M83 harbors a nuclear starburst, so it, like M51, bridges the gap between the normal spirals in our sample and more extreme starbursts like the Antennae (Fabbiano et al. 2001). A detailed study of the first observation of M83 is presented in Soria & Wu (2002, 2003). We extend their catalog by an additional 54 sources, many falling on the neighboring ACIS S2 and S4 chips.

The LF slope of M83 is quite flat, consistent with a high star formation rate in its recent past (e.g., Harris et al. 2001). The X-ray colors indicate a mix of high- and low-mass binaries with quite a lot of potential SNRs and SSSs as compared with the other galaxies in our sample. There is also the suggestion of an overabundance of soft sources near the nuclear region, indicating that these sources are indeed SNRs in the nuclear starburst region. 34% of the population exhibits long-term variability; a lower limit since the first observation was 5 times the duration
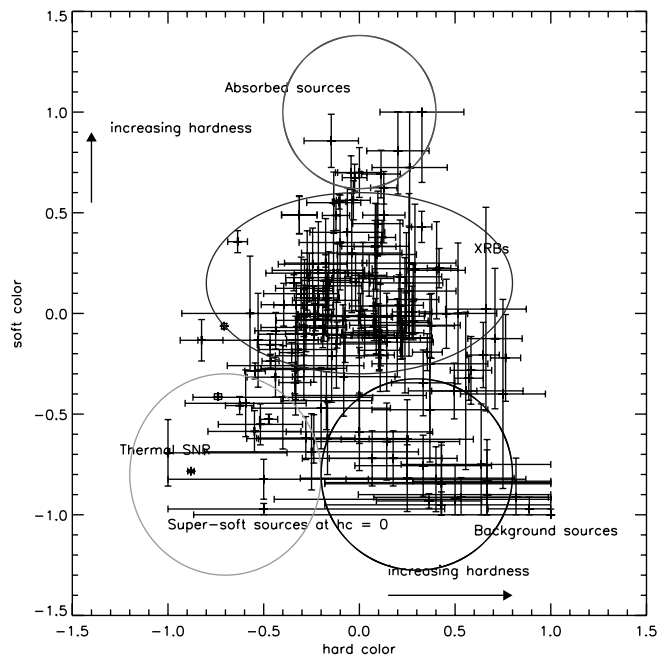
of the second. Plotted in Figures 36, 37, 38, and 39 are the LF, smoothed three-color X-ray image, optical image with X-ray source overlays, and X-ray color-color diagram. The S3 completeness limits for the two observations are 4.1×10^{36} and 1.9×10^{37} ergs s^{-1}. The FI chip completeness limits for the two observations are 5.1×10^{36} and 2.6×10^{37} ergs s^{-1}.

3.10. *M101 (NGC 5457), Scd*

M101 is the (spatially) largest galaxy in our sample at just under 1/2 a degree across and was observed for the longest single exposure (100 ks). Not surprisingly, it also contains the most point sources. Analysis of the longer *Chandra* pointing has been presented in Pence et al. (2001), which focuses on the ACIS-S3 chip. Building on their work, we include analysis of both *Chandra* observations and a set of five ACIS chips (I2, I3, S2, S3, and S4) to more than double their source catalog. Since the second *Chandra* pointing is only 1/10 the length of the first observation, many of the sources are not detected in the second and it therefore may not be too useful to compare the luminosity functions of the two observations. Since the front-illuminated ACIS CCDs have much higher detection thresholds than do the back-illuminated chips, in fitting the LFs we only consider sources above the detection thresholds for a front-illuminated CCD.

M101 contains three ultraluminous X-ray sources. One is a SSS, with almost no photons detected above 1 keV. This source exhibits extreme flaring variability. An analysis of these sources is presented in Mukai et al. (2003).

The LF slope of M101 is moderately steep. The X-ray colors indicate a mix of low- and high-mass binaries with many SNRs and SSSs. In the case of M101, we speculate that the abundance of SNR candidates is not due to a higher than average SFR but rather due to the much deeper observation of M101 as compared with the other galaxies in the sample. There is the suggestion of an overabundance of soft sources toward the nucleus, but we believe this is a selection effect due to the decreased sensitivity of the outlying front-illuminated ACIS chips to low-energy photons. Though the X-ray colors of the sources on the front-illuminated
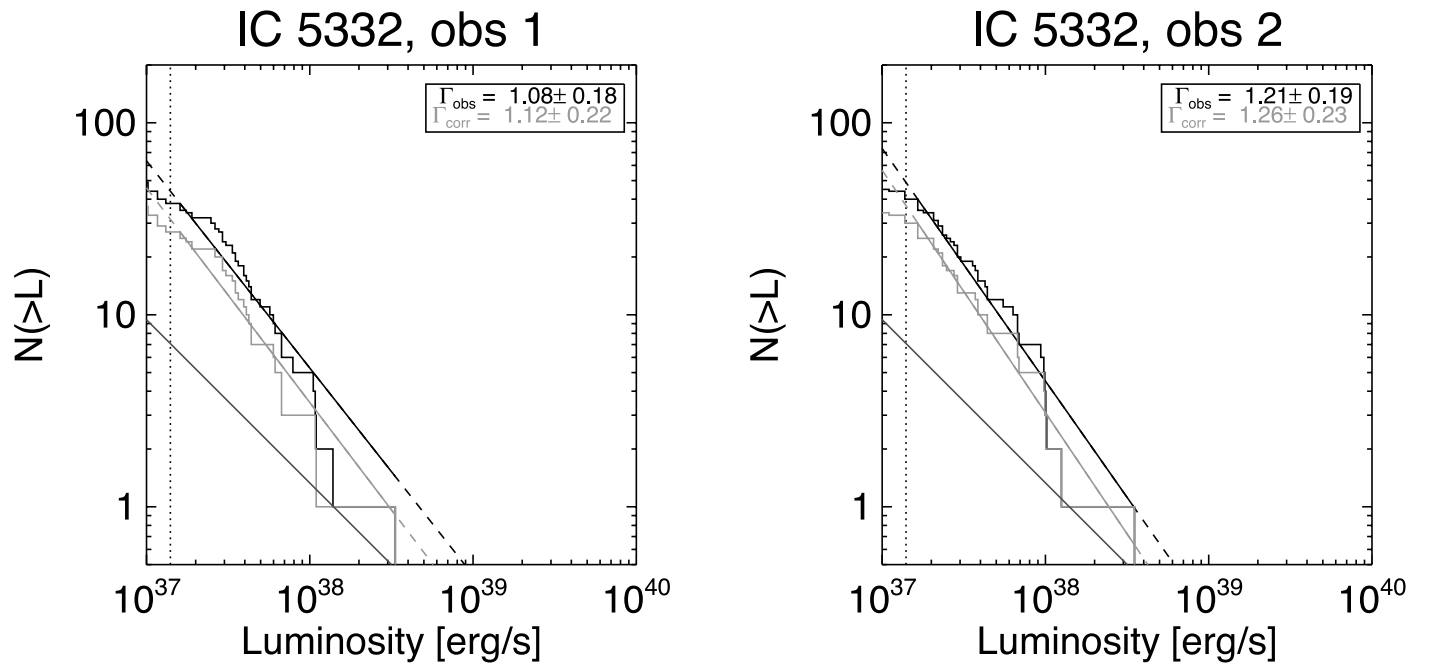
FIG. 44.—Cumulative luminosity function of the X-ray point sources in IC 5332.
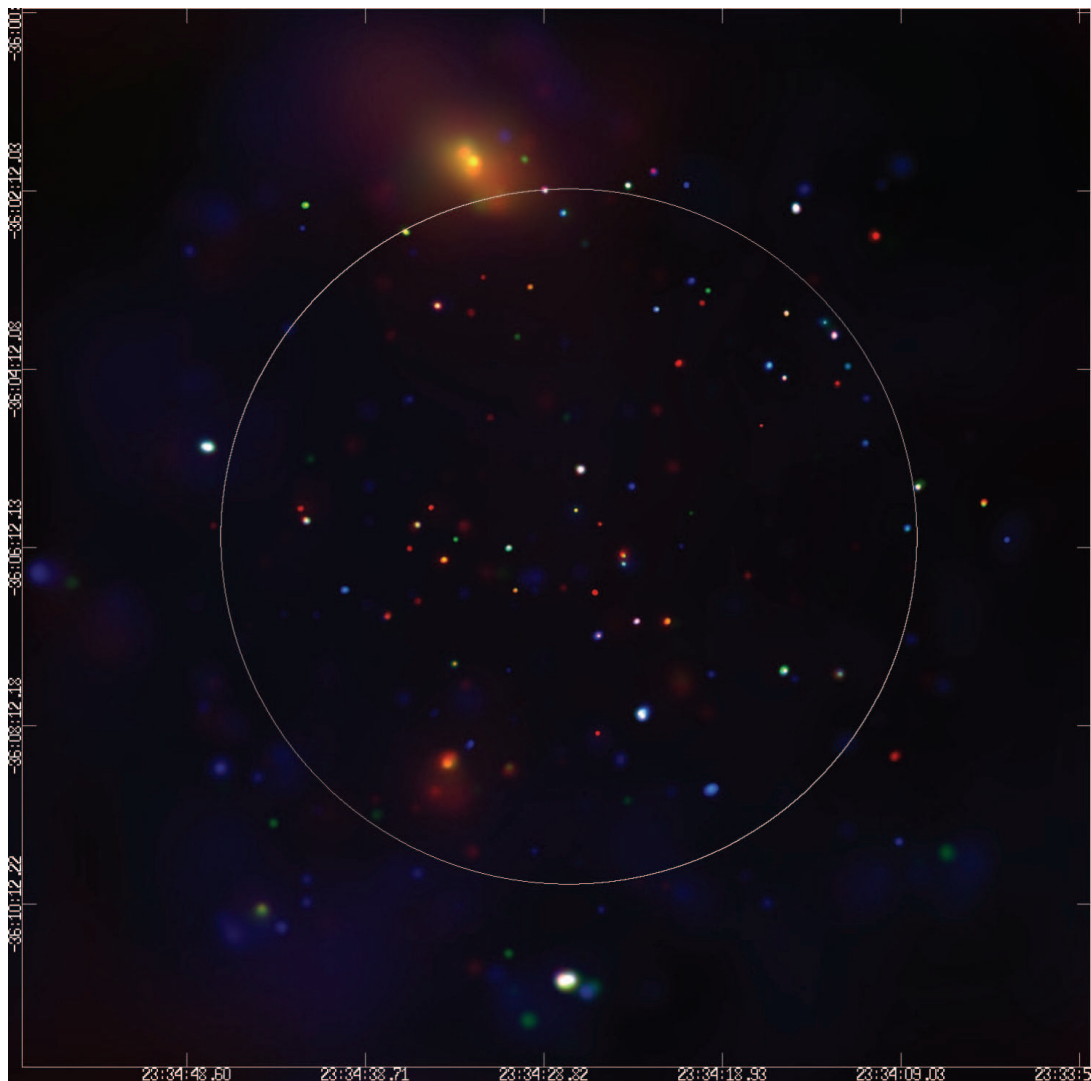

FIG. 45.—Merged *Chandra* observation of IC 5332. Adaptively smoothed. Red is 0.3–1 keV, green 1–2 keV, and blue 2–8 keV.
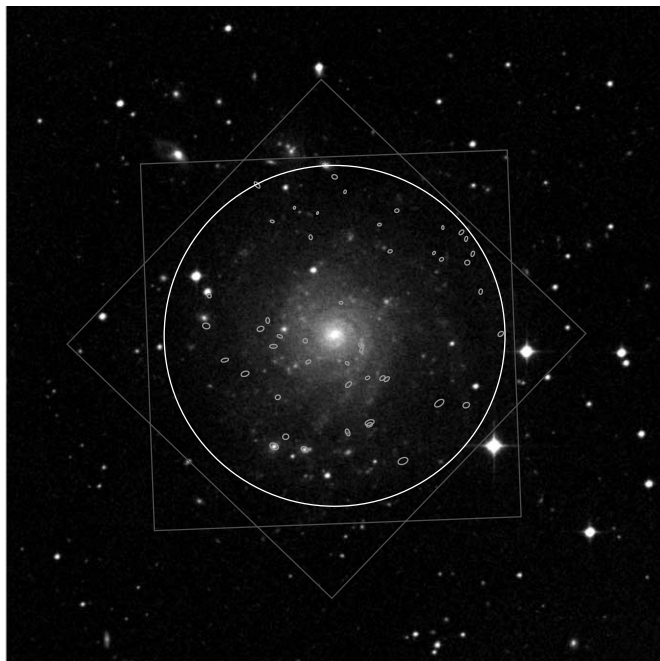
Fig. 46.—DSS optical image of IC 5332 with *Chandra* sources overlaid. The white circle is the D25 extent of the galaxy. The scale of the image is $10' \times 10'$. [*See the electronic edition of the Journal for a color version of this figure.*]

Fig. 47.—Color-color diagram of the X-ray point sources in IC 5332. [*See the electronic edition of the Journal for a color version of this figure.*]

chips have been weighted to approximate colors on the S3 chip, the detection threshold is still quite a bit higher on those chips, due both to the lower effective area at low energies of the FI chips and the large off-axis angles. 10% of the population is variable, again an extreme lower limit due to the factor of 10 difference in exposure times of the two observations. Plotted in Figures 40, 41, 42, and 43 are the LF, smoothed three-color X-ray image, optical image with X-ray source overlays, and X-ray color-color diagram. The S3 completeness limits for the two observations are 4.4×10^{36} and 4.6×10^{37} ergs s^{-1}. The FI chip completeness limits for the two observations are 6.3×10^{36} and 6.4×10^{37} ergs s^{-1}.

3.11. *IC 5332, Sd*

IC 5332 is another good Milky Way analog with emission consisting almost entirely of resolved point sources. The completeness limit for each observation is 1.4×10^{37} ergs s^{-1}. The LF slope is quite steep, and the X-ray colors indicate a mix of high- and low-mass binaries. There is no clear detection of a nuclear source. Though there is the suggestion of unresolved X-ray emission toward both the NE and SE, these are actually two background clusters of galaxies outside the radius of IC 5332. 17% of the sources exhibit long-term variability. Plotted in Figures 44, 45, 46, and 47 are the LF, smoothed three-color X-ray image, optical image with X-ray source overlays, and X-ray color-color diagram.

4. DISCUSSION

We present lists and properties of the X-ray point sources in 11 nearby spiral galaxies. Here we discuss global properties of the sample.

4.1. *Luminosity Functions*

In Kilgard et al. (2002) we discussed the relation between the slope of the discrete source luminosity functions and the star formation rate of the host galaxies as it pertained to a sample of starburst and "normal" spiral galaxies. There is a clear distinc-
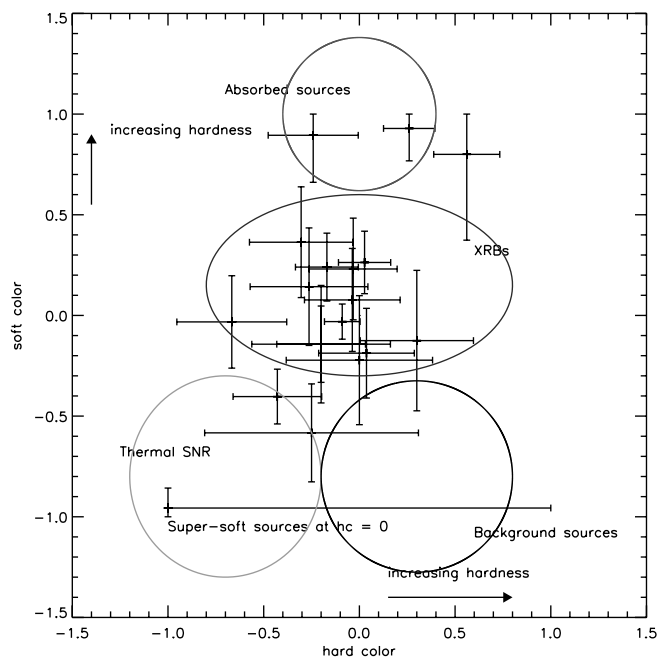
tion between the two classes: starburst galaxies have significantly flatter LFs than do normal spirals. In addition, there was the suggestion of a statistical excess of ULXs in the starburst galaxies, though it was not a statistically significant excess in all cases. Further work has been done by Colbert et al. (2003), who show that the correlation extends to early-type galaxies and that the total X-ray point source luminosity is dominated by ULXs.

As the galaxies discussed here are not starbursts, one would expect a more narrow range in LF slope, and this is indeed the case, as can be seen in Table 1. In addition, in our earlier work we noted that starburst galaxies contain an apparent excess of ULXs, whereas normal spirals did not. That trend continues in these data (Table 1), with most galaxies containing one or two ULX.

One would like to separate the bulge and disk sources for each galaxy and compare the LFs to see if a discernible difference in slope is detected due to a difference in the underlying stellar population. However, the limited number of sources in each galaxy would render any results statistically insignificant except in the case of M101, which has over 200 point sources but essentially no bulge. We instead combine the galaxies with a primarily bulge population and a primarily disk population: NGC 278, NGC 1291, NGC 2681, and NGC 4314, and M74, NGC 3184, M101, and IC 5332, respectively. For these combined LFs, we consider only the longest available *Chandra* observation for each galaxy. In addition, we use only the data above the detection threshold for the galaxy with the highest detection threshold in each group. For M101, though the observations cover 78% of the galaxy, much of that data is on the front-illuminated ACIS CCDs, which have a much higher detection threshold. For the purposes of the combined LF, we consider only the data above the detection threshold for the front-illuminated CCDs. The LF slopes are 1.14 ± 0.17 for bulge sources and 1.17 ± 0.14 for disk sources. We also combine M51, M94, and M83, as they have higher star formation rates than the rest of the sample—M51 due to the recent interaction between the galaxies, and M83 and the nuclear region of M94 due to mild nuclear starbursts. The LF slope of these

TABLE 3
VARIABILITY SIMULATIONS

Galaxy	Number of Sources[a]	Fraction of Sources[b]	Fraction of Variability[c]	Similated Variability[d]	Detected Variability[e]
NGC 278.............................	14	1.0	0.5	0.31/0.25	0.20
		0.5	0.5	0.15/0.12	
		1.0	0.2	0.04/0.04	
		0.5	0.2	0.02/0.02	
M74 (NGC 628)...................	67	1.0	0.5	0.27/0.26	0.23
		0.5	0.5	0.13/0.13	
		1.0	0.2	0.04/0.04	
		0.5	0.2	0.02/0.02	
NGC 1291............................	93	1.0	0.5	0.25/0.25	0.29
		0.5	0.5	0.12/0.13	
		1.0	0.2	0.03/0.05	
		0.5	0.2	0.01/0.03	
NGC 2681............................	23	1.0	0.5	0.37/0.38	0.43
		0.5	0.5	0.18/0.19	
		1.0	0.2	0.09/0.09	
		0.5	0.2	0.04/0.04	
NGC 3184............................	49	1.0	0.5	0.15/0.35	0.24
		0.5	0.5	0.08/0.17	
		1.0	0.2	0.01/0.08	
		0.5	0.2	0.01/0.04	
NGC 4314............................	19	1.0	0.5	0.17/0.17	0.14
		0.5	0.5	0.08/0.09	
		1.0	0.2	0.02/0.02	
		0.5	0.2	0.01/0.01	
M94 (NGC 4736).................	50	1.0	0.5	0.15/0.16	0.14
		0.5	0.5	0.08/0.08	
		1.0	0.2	0.02/0.02	
		0.5	0.2	0.01/0.01	
M51 (NGC 5194/95).............	117	1.0	0.5	0.24/0.24	0.31
		0.5	0.5	0.12/0.12	
		1.0	0.2	0.04/0.06	
		0.5	0.2	0.02/0.03	
M83 (NGC 5236).................	131	1.0	0.5	0.27/0.31	0.24
		0.5	0.5	0.13/0.15	
		1.0	0.2	0.04/0.11	
		0.5	0.2	0.02/0.05	
M101 (NGC 5457)................	208	1.0	0.5	0.14/0.13	0.10
		0.5	0.5	0.07/0.06	
		1.0	0.2	0.01/0.05	
		0.5	0.2	0.01/0.02	
IC 5332	50	1.0	0.5	0.23/0.24	0.17
		0.5	0.5	0.12/0.12	
		1.0	0.2	0.03/0.03	
		0.5	0.2	0.02/0.02	

[a] Total number of sources detected in the galaxy.
[b] Fraction of sources allowed to vary each iteration.
[c] Fraction of flux by which the sources were allowed to vary.
[d] Fraction of sources with detectable, statistically significant variability in the simulation for each *Chandra* observation.
[e] Observed variability fraction.

galaxies combined is 0.70 ± 0.06, significantly flatter than the bulge-dominated and disk-dominated subsets (see Fig. 2). This is in agreement with the conclusions in Kilgard et al. (2002) as well as those in Colbert et al. (2003) and suggests that there may be an excess of high-mass X-ray binaries (HMXBs) created by the more recent star formation as compared with those galaxies dominated by a bulge population.

4.2. *Variability*

As discussed for each galaxy, a large fraction of the source population is variable on both short and long timescales. It should be mentioned that all variability fractions quoted through-

out are, necessarily, lower limits. For the purposes of this discussion, we consider only sources whose positions are on the detector in both *Chandra* observations. Long-term variability is defined as any source that shows a clear deviation in count rate between the two observations at the 90% confidence level. As for the color classification, the Gehrels approximation is used to compute errors. To determine the range of long-term variability we would expect to detect given our data, we performed variability simulations. The source data were allowed to vary randomly by fixed quantities (10%, 20%, and 50%) and Poisson noise was added. The data were then scaled to the duration of the other *Chandra* observation and tested for statistically significant

variability at the 90% level. As can be seen in Table 3, a much larger fraction of sources must indeed be variable in order to arrive at the observed variability fractions.

In addition, we performed tests for short-term variability within each observation. Two methods were utilized: a Bayesian block routine following the method of Scargle (1998) and a simple Kolmogorov-Smirnov (KS) test. The Bayesian block method is efficient at detecting localized structures in the light curve (bursts) but is also somewhat sensitive to larger scale variability. The KS test compares the photon arrival times for a source with the flat light curve of mean flux for that source in that observation and is thus sensitive to longer timescale variability during a single observation, as compared with the Baysian block method, which is largely sensitive to flaring behavior. Results of the tests for individual sources are presented in the catalog. As determined by the Baysian block method, eight of the sources are variable at the 99% confidence level. From the KS test, 33 of the sources are variable at the 99.5% confidence level.

We have also discussed how the colors of X-ray sources may allow insight into the nature of the sources (Prestwich et al. 2003). This color sorting method, combined with the variability, should allow us to confirm if the sources fall into the coarse bins of XRBs and SNRs. Sources that are variable should, for the most part, fall outside the color-space defined as SNRs, roughly colors $HC < -0.2$ and $SC < -0.3$. As can be seen in Figure 1, the majority of sources that exhibit statistically significant variability between the two *Chandra* observations and that contain a sufficient number of counts in both observations to obtain accurate colors fall within the XRB band.

5. CONCLUSIONS

We have presented results from a survey of nearby, face-on spiral galaxies observed with *Chandra*. We have observed 11 galaxies with 22 *Chandra* observations for a total of 869 ks. The galaxies in our sample are at high Galactic latitude to minimize the absorbing column in the line of site, are nearby to minimize source confusion, and span the Hubble sequence for spirals (types 0–7). We detect 822 unique point sources in at least one observation within the D_{25} ellipses of the galaxies. A minimum of 27% of the sources exhibit detectable long- or short-term variability, indicating a source population dominated by accreting XRBs. We detect 17 ultraluminous X-ray sources, with typical rates per galaxy of 1 or 2. We apply the scheme of Prestwich et al. (2003) to determine initial source classifications for each source. The LF slopes of sources in the galaxies are correlated with the SFR, consistent with the earlier work in Kilgard et al. (2002).

This sample provides an unique data set for the further analysis of X-ray point sources in galaxies. It is the first sample of galaxies observed with *Chandra* to have been analyzed following exactly the same procedure, allowing for further study of the discrete source luminosity functions and source classification schemes. We have made progress toward the classification of X-ray sources based upon X-ray colors and variability properties, but there is still much work to be done. Analysis of the environments of the point sources within their host galaxies and comparisons with multiwavelength data are still necessary in order to more precisely determine the nature of Galactic X-ray point sources.

6. THE CATALOG

Presented here are the source lists for our sample of galaxies. The list includes source name, soft counts (0.3–1.0 keV), medium counts (1.0–2.0 keV), hard counts (2.0–8.0 keV), and total counts in each observation (0.3–8 keV), soft and hard X-ray colors, any alternative source names available from the literature, and flux and luminosities derived for each observation (also 0.3–8.0 keV). Also presented are plots of the luminosity functions, "true color" X-ray images, optical images with X-ray overlays, and color-color diagrams. In Addition, best-fit spectral parameters are presented for the brightest sources in the sample. It should be noted that the counts presented are raw, background-subtracted counts, so the count rates in sources from the same galaxy that fall on different CCDs cannot be directly compared. The colors presented have been corrected for the differences between front-illuminated and back-illuminated CCDs.

REFERENCES

Benedict, G. F., Higdon, J. L., Tollestrup, E. V., Hahn, J. M., & Harvey, P. M. 1992, AJ, 103, 757
Benedict, G. F., Smith, B. J., & Kenney, J. D. P. 1996, AJ, 111, 1861
Colbert, E., Heckman, T., Ptak, A., Strickland, D., & Weaver, K. 2003, ApJ, 602, 231
Colbert, E. J. M., & Ptak, A. F. 2002, ApJS, 143, 25
Crawford, D. F., Jauncey, D. L., & Murdoch, H. S. 1970, ApJ, 162, 405
de Costa, L. N., Pellegrini, P. S., Davis, M., Meiksin, A., Sargent, W. L. W., & Tonry, J. L. 1991, ApJS, 75, 935
de Vaucouleurs, G. 1975, ApJS, 29, 193
de Vaucouleurs, G., de Vaucouleurs, A., Corwin, H. G., Jr., Buta, R. J., Paturel, G., & Fouque, P. 1991, Third Reference Catalog of Bright Galaxies, version 3.9 (Berlin: Springer)
Eracleous, M., Shields, J. C., Chartas, G., & Moran, E. C. 2002, ApJ, 565, 108
Fabbiano, G. 1989, ARA&A, 27, 87
Fabbiano, G., & White, N. E. 2005, in Compact Stellar X-Ray Sources, (Cambridge: Cambridge Univ. Press), in press (astro-ph/0307077)
Fabbiano, G., Zezas, A., & Murray, S. S. 2001, ApJ, 554, 1035

Feldmeier, J. J., & Ciardullo, R. 1997, ApJ, 479, 231
Freeman, P. E., Kashyap, V., Rosner, R., & Lamb, D. Q. 2002, ApJS, 138, 185
Gehrels, N. 1986, ApJ, 303, 336
Giacconi, R., et al. 2001, ApJ, 551, 624
Harris, J., Calzetti, D., Gallagher III, J. S., Conselice, C. J., & Smith, D. A. 2001, AJ, 122, 3046
Huchra, J. P., Vogeley, M. S., & Geller, M. J. 1999, ApJS, 121, 287
Irwin, J. A., Sarazin, C. L., & Bregman, J. N. 2002, ApJ, 570, 152
Kilgard, R. E., Kaaret, P., Krauss, M. I., Prestwich, A. H., Raley, M. T., & Zezas, A. 2002, ApJ, 573, 138
Kong, A. K. H., DiStefano, R., Garcia, M. R., & Greiner, J. 2003, ApJ, 585, 298
Krauss, M. I., Kilgard, R. E., Garcia, M., Roberts, T., & Prestwich, A. H. 2005, ApJ, in press
Leonard, D. C., et al. 2002, AJ, 124, 2490
Mukai, K., Pence, W. D., Snowden, S. L., & Kuntz, K. D. 2003, ApJ, 582, 184
Mulder, P. S., & van Driel, W. 1993, A&A, 272, 63
Pence, W. D., Snowden, S. L., Mukai, K., & Kuntz, K. D. 2001, ApJ, 561, 189
Pogge, R. W. 1989, ApJS, 71, 433

Prestwich, A. H., Irwin, J. A., Kilgard, R. E., Krauss, M. I., Zezas, A., Primini, F., & Kaaret, P. 2003, ApJ, 595, 719

Sarazin, C. L., Irwin, J. A., & Bregman, J. N. 2000, ApJ, 544, L101

Scargle, J. D. 1998, ApJ, 504, 405

Schlegel, E. M. 2001, ApJ, 556, L25

Shirey, R., et al. 2001, A&A, 365, L195

Soria, R., & Kong, A. K. H. 2002, ApJ, 572, L33

Soria, R., & Wu, K. 2002, A&A, 384, 99

———. 2003, A&A, 410, 53

Stetson, P. B., et al. 1998, ApJ, 508, 491

Swartz, D. A., Ghosh, K. K., McCollough, M. L., Pannuti, T. G., Tennant, A. F., & Wu, K. 2003, ApJS, 144, 213

Terashima, Y., & Wilson, A. S. 2003, ApJ, 601, 735

Thim, F., Tammann, G. A., Saha, A., Dolphin, A., Sandage, A., Tolstoy, E., & Labhardt, L. 2003, ApJ, 590, 256

Tully, R. B. 1988, Nearby Galaxies Catalog (Cambridge: Cambridge Univ. Press)

Turner, J. L., & Ho, P. T. P. 1994, ApJ, 421, 122

Ⓔ

ERRATUM: "A *CHANDRA* SURVEY OF NEARBY SPIRAL GALAXIES. I. POINT SOURCE CATALOGS" (ApJS, 159, 214 [2005])

R. E. Kilgard, J. J. Cowan, M. R. Garcia, P. Kaaret, M. I. Krauss, J. C. McDowell, A. H. Prestwich, F. A. Primini, C. J. Stockdale, G. Trinchieri, M. J. Ward, and A. Zezas

Due to an oversight at the editorial offices, the published version of our paper is missing the catalog table discussed in the text. We here give this table as Table 4, with the complete machine-readable table available in the electronic edition. In the text of the article, discussions of "the catalog tables for each galaxy" should refer to Table 4, given below.

Online material: machine-readable table

TABLE 4
Chandra Source Properties

ID	R.A. (J2000)	Decl. (J2000)	Soft Counts	Medium Counts	Hard Counts	Total Counts	Soft Color	Hard Color	Flux $(10^{-16}$ ergs s^{-1} cm$^{-2})$	Luminosity $(10^{36}$ ergs s$^{-1})$
				NGC 278						
CXOU J005202.2+473316	00 52 02.15	+47 33 16.33	0.93 ± 2.30	5.60 ± 3.52	2.80 ± 2.88	9.33 ± 4.18	$0.71^{+0.29}_{-0.62}$	$-0.33^{+0.54}_{-0.54}$	10.45 ± 4.68	25.58 ± 11.44
CXOU J005202.7+473308	00 52 02.72	+47 33 07.78	17.98 ± 5.33	21.84 ± 5.75	16.59 ± 5.16	56.41 ± 8.56	$0.10^{+0.20}_{-0.20}$	$-0.14^{+0.20}_{-0.20}$	85.64 ± 13.00	209.55 ± 31.80
CXOU J005203.4+473312	00 52 03.36	+47 33 12.15	2.98 ± 2.93	2.46 ± 2.79	4.35 ± 3.26	9.79 ± 4.25	$-0.10^{+0.74}_{-0.74}$	$0.28^{+0.63}_{-0.63}$	10.82 ± 4.69	26.46 ± 11.48
CXOU J005203.4+473255	00 52 03.43	+47 32 55.27	17.39 ± 5.26	35.27 ± 7.00	13.13 ± 4.73	65.79 ± 9.16	$0.34^{+0.16}_{-0.16}$	$-0.46^{+0.16}_{-0.16}$	94.19 ± 13.11	230.46 ± 32.08
CXOU J005203.9+473310	00 52 03.85	+47 33 09.87	15.13 ± 4.98	28.21 ± 6.38	7.69 ± 3.90	51.03 ± 8.20	$0.30^{+0.18}_{-0.18}$	$-0.57^{+0.19}_{-0.19}$	77.35 ± 12.42	189.25 ± 30.40

NOTES.—Table 4 is published in its entirety in the electronic edition of the *Astrophysical Journal Supplement*. A portion is shown here for guidance regarding its form and content. The full machine-readable table contains additional columns, including the results from the second *Chandra* observation, and rows for all eleven galaxies from the paper.